REPORT DOCUMENTATION PAGE

AFRL-SR-BL-TR-98-

0694

1-0188

1. AGENCY USE ONLY *(Leave blank)*	2. REPORT DATE	3. REPORT TYPE AND DATES COVERED
	August 14, 1998	Final, May 15, 1995 – August 15, 1998

4. TITLE AND SUBTITLE	5. FUNDING NUMBERS
Nonlinear Modeling, Analysis, and Control of Turbomachinery Stall Flutter	F49620 – 95 – C – 0035

6. AUTHOR(S)

George Scott Copeland
Gonzalo Rey

7. PERFORMING ORGANIZATION NAME(S) AND ADDRESS(ES)	8. PERFORMING ORGANIZATION REPORT NUMBER
United Technologies Research Center 411 Silver Lane East Hartford, CT. 06108	

9. SPONSORING /MONITORING AGENCY NAME(S) AND ADDRESS(ES)	10. SPONSORING /MONITORING AGENCY REPORT NUMBER
Air Force Office of Scientific Research 110 Duncan Avenue, Suite B115	

11. SUPPLEMENTARY NOTES

12a. DISTRIBUTION/AVAILABILITY STATEMENT	12b. DISTRIBUTION CODE
Unlimited	

13. ABSTRACT *(Maximum 200 words)*

Abstract

The linear and nonlinear dynamic behavior of flexibly-bladed turbomachines is presented. The analytical description is based on matching a two dimensional, incompressible flow field across a semi-actuator disk representation of a flexible rotor and a rigid stator. The aerodynamic loading on the rotor is derived using control volume formulations applied to discrete blade passages allowing consideration of finite interblade phase angles. Depending on operating parameters, the model exhibits behaviors classified as surge, rotating stall, and stall flutter which are qualitatively consistent with experimentally observed results.

The formulation provides a tractable, nonlinear state-space description of the dynamics responsible for surge, rotating stall, flutter, and their interaction. An analysis is performed for system parameters representative of a laboratory-scale fan test facility. The behavior of the operability-limiting instability modes is examined using time simulations, eigenvalue analysis and stability diagrams.

14. SUBJECT TERMS			15. NUMBER OF PAGES
Flutter, Stall, Aeroelasticity, Turbomachinery, Stability. Bifurcation			68
			16. PRICE CODE

17. SECURITY CLASSIFICATION OF REPORT	18. SECURITY CLASSIFICATION OF THIS PAGE	19. SECURITY CLASSIFICATION OF ABSTRACT	20. LIMITATION OF ABSTRACT
Unclassified	Unclassified	Unclassified	UL

NSN 7540-01-280-5500

Standard Form 298 (Rev. 2-89)

AFOSR Contractor Final Report

Nonlinear Modeling, Analysis, and Control of Turbomachinery Stall Flutter

August 14, 1998

George Scott Copeland
Gonzalo Rey
United Technologies Research Center
Mail Stop 129-15
411 Silver Lane East Hartford, Connecticut 06108

19981113 064

DTIC QUALITY INSPECTED 4

Abstract

The linear and nonlinear dynamic behavior of flexibly-bladed turbomachines is presented. The analytical description is based on matching a two dimensional, incompressible flow field across a semi-actuator disk representation of a flexible rotor and a rigid stator. The aerodynamic loading on the rotor is derived using control volume formulations applied to discrete blade passages allowing consideration of finite interblade phase angles. Depending on operating parameters, the model exhibits behaviors classified as surge, rotating stall, and stall flutter which are qualitatively consistent with experimentally observed results.

The formulation provides a tractable, nonlinear state-space description of the dynamics responsible for surge, rotating stall, flutter, and their interaction. An analysis is performed for system parameters representative of a laboratory-scale fan test facility. The behavior of the operability-limiting instability modes is examined using time simulations, eigenvalue analysis and stability diagrams.

1

Contents

List of Figures

List of Tables

1 Introduction

Surge, rotating stall, and flutter are instability phenomena that fundamentally constrain the design and operation of modern gas turbine engines. Classically, these different forms of compression system instabilities have been categorized based on observations of observations of limit cycle oscillations. *Rotating stall* and *surge* are primarily aerodynamic instabilities. *Flutter* is an aeroelastic instability involving blade motion which can occur in various regions of the compressor performance map. In addition to instability, the forced response of flutter modes is extremely important. A lightly-damped flutter mode can be excited by gusts or by defects in the inlet flow resulting in the accumulation of fatigue.

The purpose of the research effort is to provide a framework to develop and analyze nonlinear dynamic models of flexibly-bladed turbomachines where surge, rotating stall, and flutter can be studied as coupled instability mechanisms. One cannot expect good predictive capability from such a model, rather the objective is to determine qualitatively the trends in system stability and nonlinear dynamics as system parameters are varied. Reduced-order models may be used to test some of the simplifications typical in more comprehensive computational models such as the modeling of losses, choice of the inlet boundary condition, and the influence of downstream bladerows. Another role for reduced-order models is in the development of experimental methodology and in the interpretation of data. Finally, reduced-order models are well suited for studies in active and passive control.

Reduced-order, nonlinear compression system models have been constructed based on an actuator disk approach. A hierarchy of models has been developed which includes in order of increasing complexity: (i) a compressor model with an empirically-motivated polynomial characteristic, (ii) a compressor model with a characteristic determined from the ideal pressure rise and lagged losses, (iii) the incorporation of an inter-bladerow space between the rotor and stator, and (iv) the incorporation of rotor blade flexibility. The models are in the form of differential-algebraic equations constructed from idealized governing equations using symbolic algebra. The framework is such that changes to the physical modeling can be easily incorporated.

Analysis has focused on the determination of stability boundaries through generalized eigensystem analyses and the determination of the initial post-instability dynamics. These two features provide the dominant criteria for predicting the operating regime. Principal results from the analysis are the demonstration that the relative damping of the flutter modes is determined most strongly by the plunge to twist ratio of the blades. System stability has been examined with respect to operating conditions including shaft speed, nominal mass flow, inlet temperature and flight speed. It is also shown that loss and deviation may have a significant effect on flutter damping. Numerical simulations have been used to demonstrate that stable flutter and stall limit cycles may coexist. Lastly, linear analysis has been used to compute pole-zero dia-

grams and Bode plots demonstrating how one would use the models to support the planning of experiments.

2 Physical modeling

The present model is a further development of the work of Gysling and Myers [2]. The bladerows are represented by actuator disks, the flow fields are two-dimensional and incompressible, and the surge dynamics are described (effectively) by a Helmholtz resonator. The system variables and parameters are listed in tables 1 and 2 respectively. Wong [8] improved upon the formulation of Gysling and Myers primarily by accounting for nonlinear dependence on interblade phase angle. The present model differs from that of Gysling and Myers and that of Wong as follows:

- In the formulation of the deforming rotor control volume, it is shown that the width of the control volume is immaterial as one should expect from an actuator disk. In those earlier works, a representative blade passage was chosen as the control volume.

- The present model accounts for control volume deformation in the energy equation. The earlier works do not.

- An inter-bladerow space has been incorporated for the purpose of parameterizing the relative coupling between the rotor and the stator.

- Inlet total pressure is introduced as a parameter.

- Mass flow actuation has been incorporated for the purpose of supporting system identification and control experiments.

The flow field equations are linearized about a condition of axisymmetric flow. This allows us to solve for the axial dependence of the non-axisymmetric flow perturbation. The basic variables of the model are then the components of velocity and pressure, as functions of the azimuthal angle and time, at five discrete axial stations: the rotor leading edge, the rotor trailing edge, just upstream from the mass flow actuator, just downstream from the mass flow actuator, the stator leading edge, and the stator trailing edge.

Matching conditions across the actuator disks representing the bladerows are given by the general expressions for the conservation of mass, momentum, and energy. The equations are closed using strong assumptions about flow kinematics, *i.e.* exit flow is fixed to the metal angle of the blade plus a known deviation. There is no assumption that perturbations are small and the resulting governing equations are nonlinear including transcendental functions of the flow variables.

The key assumptions behind the model are incompressible, two-dimensional modeling of the flow, actuator disk representation of the bladerows, and the

6

Table 1: List of system variables

ϕ_1	axial velocity at the rotor leading edge.
v_1	azimuthal velocity at the rotor leading edge.
p_1	pressure at the rotor leading edge.
ϕ_{2a}	axial velocity at the rotor trailing edge.
v_{2a}	azimuthal velocity at the rotor trailing edge.
p_{2a}	pressure at the rotor trailing edge.
ϕ_{2b}	axial velocity just upstream of the mass flow actuator.
v_{2b}	azimuthal velocity just upstream of the mass flow actuator.
p_{2b}	pressure just upstream of the mass flow actuator.
ϕ_{2c}	axial velocity at the stator leading edge.
v_{2c}	azimuthal velocity at the stator leading edge.
p_{2c}	pressure at the stator leading edge.
ϕ_3	axial velocity at the stator trailing edge.
p_3	pressure at the stator trailing edge.
p_p	pressure in the exit plenum.
$\mathbf{F}$	force (vector) exerted on the blade passage by the flow.
L_r	rotor loss.
L_s	stator loss.
q	blade plunge.
α	blade twist.
B_k	time dependent coefficient in inter-bladerow space streamfunction.
C_k	time dependent coefficient in inter-bladerow space streamfunction.
ω	vorticity at rotor trailing edge.
h	vorticity lag.

assumptions on flow kinematics. Wong [8] has compared predictions of a similar model to two-dimensional compressible simulations past an isolated blade row. He found that reduced-order model was suitable for stability predictions for Mach number less than 0.8, solidity greater than 8, and reduced frequency less than 0.15.

2.1 Inlet duct

The upstream flow field is assumed to be irrotational and incompressible. The system is assumed to draw flow from a reservoir with constant total pressure P_{atm}. Finite inlet effects are modeled by assuming two-dimensional flow in a slab whose thickess varies axially but the nominal radius of which is constant as suggested by Greitzer [1]. A sketch of the idealized geometry and the flow control volume are shown in figure 1. The governing fluid dynamical equations are the conservation of mass and momentum.

For the control volume sketched in figure 1, conservation of mass is expressed

Table 2: List of system parameters

P_{atm}	atmospheric pressure.
α_{inlet}	inlet geometry parameter.
L_{inlet}	actual length of inlet duct.
L_{exit}	actual length of exit duct.
c_{s}	stator chord.
τ_{r}	time scale for rotor loss.
τ_{s}	time scale for stator loss.
β_{r}	trailing edge metal angle of rotor.
β_{zr}	zero-incidence angle of rotor leading edge.
β_{zs}	zero-incidence angle of stator leading edge.
$L_{\text{r1}}, L_{\text{r2}}, L_{\text{r3}}$	coefficients of the empirical rotor loss function.
$L_{\text{s1}}, L_{\text{s2}}, L_{\text{s3}}$	coefficients of the empirical stator loss function.
Δ_1, Δ_2	coefficients of the empirical rotor deviation function.
B	Greitzer-B parameter (surge).
C_d	plenum loss coefficient.
A	throttle parameter.
L_{ibs}	length of inter-bladerow space.
N_b	number of blades
c_{r}	rotor chord.
ξ_{ea}	position of the elastic axis divided by chord.
ξ_{cg}	position of the center of gravity divided by chord.
ξ_{cp}	position of the center of pressure divided by chord.
ϵ	rotational inertia divided by chord.
D	blade mass.
Q_b	frequency of pure bending (nondimensionalized by Ω_{shaft}^2).
Q_t	frequency of pure twist (nondimensionalized by Ω_{shaft}^2).
ζ_b	structural damping of bending mode.
ζ_t	structural damping of torsion mode.
γ_{r}	stagger angle of rotor.
γ_{s}	stagger angle of stator.
ξ	actuator mass flow.
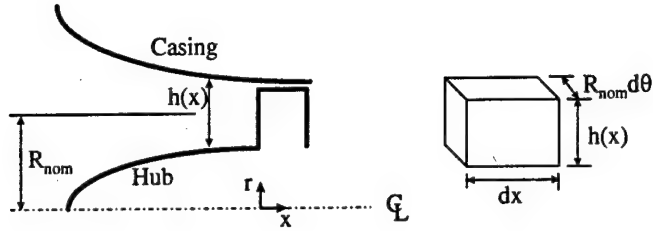
Figure 1: Sketch of idealized inlet and control volume.

by the equation

$$\frac{\partial}{\partial x}(\rho U h)R_{\text{nom}}\,dx\,d\theta + \frac{1}{R_{\text{nom}}}\frac{\partial}{\partial \theta}(\rho V h)R_{\text{nom}}\,dx\,d\theta = 0,$$

or

$$\frac{\partial}{\partial x}(Uh) + \frac{\partial}{\partial \theta}(Vh) = 0,$$

where lengths have been nondimensionalized with respect to the nominal radius. Considering perturbations about an axisymmetric state,

$$
\begin{aligned}
U &= \Phi(x,t) + \phi(x,\theta,t) \\
V &= v(x,\theta,t) \\
h &= h(x),
\end{aligned}
$$

the mass conservation equation may be expressed to first order

$$\frac{\partial}{\partial x}(\Phi h) = 0,$$

$$\frac{\partial \phi}{\partial x}h + \phi\frac{\partial h}{\partial x} + h\frac{\partial v}{\partial \theta} = 0.$$

For an irrotational flow, the perturbations may be expressed

$$\phi = \frac{\partial F}{\partial x}$$

9

$$v = \frac{\partial F}{\partial \theta},$$

and the mass conservation in terms of the velocity potential is given by

$$h\nabla^2 F + \frac{\partial F}{\partial x}\frac{dh}{dx} = 0.$$

If h is constrained to depend exponentially on x,

$$h(x) = \frac{1}{2}e^{-2\alpha_{\text{inlet}}x},$$

then F will also have solutions in exponential form,

$$F = F_n e^{k_n x} e^{in\theta},$$

where

$$k_n^2 - 2\alpha_{\text{inlet}}k_n - n^2 = 0.$$

Clearly the perturbations must decay as $x \to -\infty$, hence

$$k_n = \alpha_{\text{inlet}} + \sqrt{\alpha_{\text{inlet}}^2 + n^2}.$$

Applying the conditions of irrotationality at the rotor face, ϕ_1 and v_1 are related by the equations

$$(k_n - 2\alpha_{\text{inlet}})\phi_{1n} + inv_{1n} = 0. \tag{1}$$

For the control volume sketched in figure 1, conservation of momentum is expressed by the equation

$$\frac{\partial}{\partial t}\int_x^{x+dx} \rho U h \, dx = -\left(p + \frac{1}{2}\rho U^2\right)h,$$

which when linearized and applied at the rotor face yields

$$\frac{\dot{\phi}_{1n}}{k_n - 2\alpha_{\text{inlet}}} = -(p_{1n} + \Phi_1 \phi_{1n}). \tag{2}$$

The axisymmetric variables are assumed to be related through a momentum equation through a finite-length, uniform duct,

$$\left(P_{\text{atm}} - \frac{1}{2}\Phi_1^2\right) - P_1 = L_{\text{inlet}}\dot{\Phi}_1. \tag{3}$$

10

2.2 Blade passage deformation

The blade loading and matching conditions across the actuator disk are derived by considering a control volume corresponding to the passage between two adjacent blades. The control volume will deform of course with blade deflection. Deformation of the leading and trailing edge boundaries directly affects the conservation of mass, momentum, and energy in the control volume. The control volume is sketched in figure 2 and the positive sense of blade deflection is indicated in figure 3.
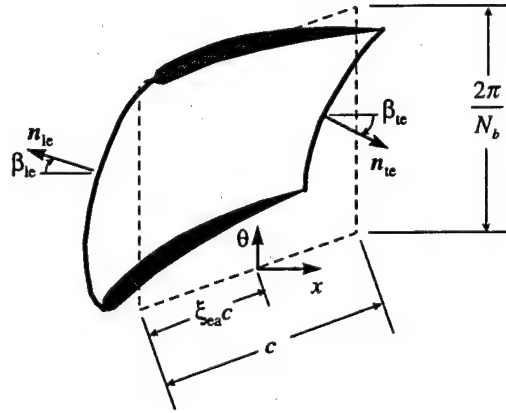
Figure 2: Definition sketch for blade passage control volume.

The deflections of the actuator disk are defined such that the actual blade deflections may be obtained simply by collocation. The twist of blade i, for example is given by

$$\alpha\left(\frac{2\pi(i-1)}{N_b}, t\right).$$

Choosing the undeflected elastic axis of the first blade as the origin, the coordinates of the leading and trailing edges are given by

$$
\begin{aligned}
x_{le} &= -q\sin\gamma_r - \xi_{ea}c\cos(\gamma_r - \alpha) \\
\theta_{le} &= \theta + q\cos\gamma_r - \xi_{ea}c\sin(\gamma_r - \alpha) \\
x_{te} &= -q\sin\gamma_r + (1 - \xi_{ea})c\cos(\gamma_r - \alpha) \\
\theta_{te} &= \theta + q\cos\gamma_r + (1 - \xi_{ea})c\sin(\gamma_r - \alpha).
\end{aligned}
$$

11
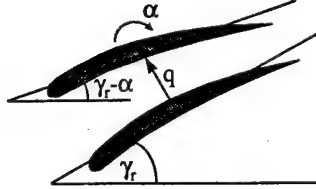
Figure 3: Definition sketch for blade deflection indicating positive sense of twist α and plunge q. The location of the elastic axis is indicated by the circle.

The outward normal vectors are given by

$$
\begin{aligned}
\mathbf{n}_{\text{le}} &= -\cos\beta_{\text{le}}\mathbf{i} + \sin\beta_{\text{le}}\mathbf{j} \\
\mathbf{n}_{\text{te}} &= \cos\beta_{\text{te}}\mathbf{i} - \sin\beta_{\text{te}}\mathbf{j},
\end{aligned}
$$

where the angles β_{le} and β_{te} are given by

$$
\begin{aligned}
\tan\beta_{\text{le}} &= \frac{\partial x_{\text{le}}/\partial\theta}{\partial\theta_{\text{le}}/\partial\theta} \\
\tan\beta_{\text{te}} &= \frac{\partial x_{\text{te}}/\partial\theta}{\partial\theta_{\text{te}}/\partial\theta}.
\end{aligned}
$$

The path lengths along the leading and trailing edges are given by

$$
\begin{aligned}
\frac{\partial s_{\text{le}}}{\partial\theta} &= \sqrt{\left(\frac{\partial x_{\text{le}}}{\partial\theta}\right)^2 + \left(\frac{\partial\theta_{\text{le}}}{\partial\theta}\right)^2} \\
\frac{\partial s_{\text{te}}}{\partial\theta} &= \sqrt{\left(\frac{\partial x_{\text{te}}}{\partial\theta}\right)^2 + \left(\frac{\partial\theta_{\text{te}}}{\partial\theta}\right)^2}.
\end{aligned}
$$

It is assumed that the exit angle of the flow is fixed by the metal angle of the deflected blade plus some deviation. The deviation and also the quasi-static

12

total pressure loss are assumed to be functions of the incidence angle. The flow geometry is sketched in figure 4. The relative velocity between the flow and the leading edge is given by

$$\mathbf{v}_{r,le} = (\phi_1 \mathbf{i} + v_1 \mathbf{j}) - \left(\frac{\partial}{\partial t} - \frac{\partial}{\partial \theta}\right)(x_{le}\mathbf{i} + \theta_{le}\mathbf{j});$$

The rotor incidence angle is then

$$\alpha_{inc,r} = \tan^{-1}\left(\frac{\mathbf{v}_{r,le} \cdot \mathbf{j}}{\mathbf{v}_{r,le} \cdot \mathbf{i}}\right) - \beta_{zr} + \alpha,$$

where β_{zr} is the zero incidence angle of the undeflected blade. Similarly, the relative velocity between the flow and the trailing edge is

$$\mathbf{v}_{r,te} = (\phi_{2a}\mathbf{i} + v_{2a}\mathbf{j}) - \left(\frac{\partial}{\partial t} - \frac{\partial}{\partial \theta}\right)(x_{te}\mathbf{i} + \theta_{te}\mathbf{j}).$$

The kinematic constraint on the exit flow angle is then

$$v_{2a} - \left(\frac{\partial}{\partial t} - \frac{\partial}{\partial \theta}\right)\theta_{te} = \left[\phi_{2a} - \left(\frac{\partial}{\partial t} - \frac{\partial}{\partial \theta}\right)x_{te}\right]\tan(\beta_r - \alpha + \Delta), \qquad (4)$$

where β_r is the metal angle of the trailing edge and the deviation is assumed to be given by

$$\Delta = \Delta_1 \alpha_{inc,r} + \Delta_2.$$

2.3   Conservation of mass across the rotor

Conservation of mass within the deforming control volume may be expressed as follows:

$$\frac{\partial}{\partial t}\int \rho dV + \int \rho(\mathbf{v}_r \cdot \mathbf{n})\, dS = 0.$$

The subscript r on the velocity vector indicates velocity with respect to the moving boundary. The time-derivative on the volume integral is to be taken in the rotor frame. The present model is two-dimensional, incompressible, and mass flux occurs over the leading and trailing-edge boundaries only, hence the mass conservation equation may be expressed

$$\left(\frac{\partial}{\partial t} - \frac{\partial}{\partial \theta}\right)\int_{\theta_1}^{\theta_2} \frac{\partial V}{\partial \theta}\, d\theta + \int_{\theta_1}^{\theta_2}(\mathbf{v}_r \cdot \mathbf{n})\frac{\partial S}{\partial \theta}\, d\theta = 0,$$

or

$$\left(\frac{\partial}{\partial t} - \frac{\partial}{\partial \theta}\right)\frac{\partial V}{\partial \theta} + (\mathbf{v}_{r,le} \cdot \mathbf{n}_{le})\frac{\partial s_{le}}{\partial \theta} + (\mathbf{v}_{r,te} \cdot \mathbf{n}_{te})\frac{\partial s_{te}}{\partial \theta} = 0, \qquad (5)$$

where

$$\frac{\partial V}{\partial \theta} = c\cos(\gamma_r - \alpha)\frac{1}{2}\left(\frac{\partial s_{le}}{\partial \theta} + \frac{\partial s_{te}}{\partial \theta}\right).$$
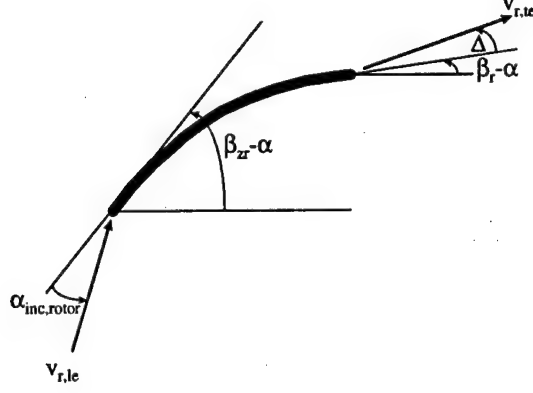
13

Figure 4: Geometry of leading and trailing-edge flow.

2.4 Conservation of momentum across the rotor

Conservation of momentum within a control volume may be expressed

$$\frac{\partial}{\partial t} \int \rho \mathbf{v} dV + \int \rho \mathbf{v} \left(\mathbf{v}_r \cdot \mathbf{n} \right) dS + \int p \mathbf{n} dS = -\mathbf{F}.$$

Applying this equation to the deforming blade passage yields

$$\left(\frac{\partial}{\partial t} - \frac{\partial}{\partial \theta} \right) \int_{\theta_1}^{\theta_2} \mathbf{v} \frac{\partial V}{\partial \theta} d\theta + \int_{\theta_1}^{\theta_2} \left[\mathbf{v} \left(\mathbf{v}_r \cdot \mathbf{n} \right) + p\mathbf{n} \right] \frac{\partial S}{\partial \theta} d\theta = - \int_{\theta_1}^{\theta_2} \frac{\partial \mathbf{F}}{\partial \theta} d\theta,$$

or

$$\left(\frac{\partial}{\partial t} - \frac{\partial}{\partial \theta} \right) \left(\mathbf{v} \frac{\partial V}{\partial \theta} \right) + \left[\mathbf{v}_{le} \left(\mathbf{v}_{r,le} \cdot \mathbf{n}_{le} \right) + p_{le} \mathbf{n}_{le} \right] \frac{\partial s_{le}}{\partial \theta}$$
$$+ \left[\mathbf{v}_{te} \left(\mathbf{v}_{r,te} \cdot \mathbf{n}_{te} \right) + p_{te} \mathbf{n}_{te} \right] \frac{\partial s_{te}}{\partial \theta} = - \frac{\partial \mathbf{F}}{\partial \theta}, \qquad (6)$$

where

$$F = \int_{\theta_1}^{\theta_2} \frac{\partial \mathbf{F}}{\partial \theta} d\theta$$

14

is the force exerted on the control volume boundaries by the fluid and

$$
\begin{aligned}
\mathbf{v}_{\text{le}} &= \phi_1 \mathbf{i} + (1 + V_1)\mathbf{j} \\
\mathbf{v}_{\text{te}} &= \phi_{2a}\mathbf{i} + (1 + V_{2a})\mathbf{j} \\
p_{\text{le}} &= p_1 \\
p_{\text{te}} &= p_{2a}.
\end{aligned}
$$

Additionally, the velocity within the control volume has been approximated by the average of the leading and trailing-edge flow velocities,

$$
\mathbf{v} = \frac{1}{2}(\mathbf{v}_{\text{le}} + \mathbf{v}_{\text{te}}).
$$

2.5 Conservation of energy across the rotor

Conservation of energy within a control volume may be expressed

$$
\frac{\partial}{\partial t} \int \frac{1}{2}\rho v^2 \, dV + \int \left(p + \frac{1}{2}\rho v^2\right)(\mathbf{v}_{\text{r}} \cdot \mathbf{n})\, dS = -\mathbf{F} \cdot \mathbf{v} + \dot{Q}.
$$

Applying this equation to the deforming blade passage yields

$$
\left(\frac{\partial}{\partial t} - \frac{\partial}{\partial \theta}\right) \int_{\theta_1}^{\theta_2} \frac{1}{2}v^2 \frac{\partial V}{\partial \theta}\, d\theta + \int_{\theta_1}^{\theta_2} \left(p_{\text{le}} + \frac{1}{2}v_{\text{le}}^2 - L_{\text{r}}\right)(\mathbf{v}_{\text{r,le}} \cdot \mathbf{n}_{\text{le}})\frac{\partial s_{\text{le}}}{\partial \theta}\, d\theta
$$

$$
+ \int_{\theta_1}^{\theta_2} \left(p_{\text{te}} + \frac{1}{2}v_{\text{te}}^2\right)(\mathbf{v}_{\text{r,te}} \cdot \mathbf{n}_{\text{te}})\frac{\partial s_{\text{te}}}{\partial \theta}\, d\theta = -\int_{\theta_1}^{\theta_2} \frac{\partial \mathbf{F}}{\partial \theta} \cdot \mathbf{v}_{\text{cv}}\, d\theta,
$$

or

$$
\left(\frac{\partial}{\partial t} - \frac{\partial}{\partial \theta}\right) \frac{1}{2}v^2 \frac{\partial V}{\partial \theta} + \left(p_{\text{le}} + \frac{1}{2}v_{\text{le}}^2 - L_{\text{r}}\right)(\mathbf{v}_{\text{r,le}} \cdot \mathbf{n}_{\text{le}})\frac{\partial s_{\text{le}}}{\partial \theta}
$$

$$
+ \left(p_{\text{te}} + \frac{1}{2}v_{\text{te}}^2\right)(\mathbf{v}_{\text{r,te}} \cdot \mathbf{n}_{\text{te}})\frac{\partial s_{\text{te}}}{\partial \theta} = -\frac{\partial \mathbf{F}}{\partial \theta} \cdot \mathbf{v}_{\text{cv}}, \tag{7}
$$

where L_{r} represents a loss in leading-edge total pressure to account for nonconservative processes. The velocity of the control volume is approximated by the average of the velocities of the leading and trailing-edge boundaries.

$$
\mathbf{v}_{\text{cv}} = \left(\frac{\partial}{\partial t} - \frac{\partial}{\partial \theta}\right)\left(\frac{x_{\text{le}} + x_{\text{te}}}{2}\mathbf{i} + \frac{\theta_{\text{le}} + \theta_{\text{te}}}{2}\mathbf{j}\right) + \mathbf{j}.
$$

2.6 Blade dynamics

The blade dynamics are modeled using a typical section with inertial and aerodynamic coupling between twist and plunge. The lift force is assumed to act at the center of pressure which is assumed constant,

$$
F_l = [\mathbf{F}(\theta + \pi/N_b, t) - \mathbf{F}(\theta - \pi/N_b, t)] \cdot [-\sin(\gamma_{\text{r}} - \alpha)\mathbf{i} + \cos(\gamma_{\text{r}} - \alpha)\mathbf{j}],
$$

15

and the aerodynamic moment is applied at the elastic axis, which is also assumed constant,

$$M = F_l(\xi_{\mathrm{ea}} - \xi_{\mathrm{cp}})c.$$

The blade bending equation is then

$$\left(\frac{\partial}{\partial t} - \frac{\partial}{\partial \theta}\right)^2 q + (\xi_{\mathrm{ea}} - \xi_{\mathrm{cg}})c \left(\frac{\partial}{\partial t} - \frac{\partial}{\partial \theta}\right)^2 \alpha$$

$$+2\zeta_b Q_b \left(\frac{\partial}{\partial t} - \frac{\partial}{\partial \theta}\right) q + Q_b^2 q = \frac{F_l}{D}, \tag{8}$$

and the blade twist equation is

$$\left(\frac{\partial}{\partial t} - \frac{\partial}{\partial \theta}\right)^2 \alpha + \frac{(\xi_{\mathrm{ea}} - \xi_{\mathrm{cg}})cD}{I_{\mathrm{ea}}} \left(\frac{\partial}{\partial t} - \frac{\partial}{\partial \theta}\right)^2 q$$

$$+2\zeta_t Q_t \left(\frac{\partial}{\partial t} - \frac{\partial}{\partial \theta}\right) \alpha + Q_t^2 \alpha = \frac{M}{I_{\mathrm{ea}}}, \tag{9}$$

where

$$I_{\mathrm{ea}} = D(\xi_{\mathrm{ea}} - \xi_{\mathrm{cg}})^2 c^2 + Dc^2\epsilon^2.$$

2.7   Flow field in the inter-bladerow space

In the inter-blade space, the perturbation to the axisymmetric flow is modeled as a vortical inviscid flow. The axisymmetric components of velocity V and Φ remain constant over the interblade space,

$$\Phi_{2a} = \Phi_{2b} \tag{10}$$

$$V_{2a} = V_{2b}; \tag{11}$$

the axisymmetric component of the pressure field may be found from the balance of energy,

$$P_{2a} - P_{2b} = L_{\mathrm{ibs}} \frac{d\Phi_{2a}}{dt}. \tag{12}$$

The velocity and pressure perturbation fields at the upstream and downstream ends of the inter-bladerow space will be related to each other through the streamfunction Ψ and the associated vorticity field ω,

$$-\nabla^2 \Psi = \omega,$$

$$\frac{D\omega}{Dt} = \frac{\partial \omega}{\partial t} + \Phi_{2a}\frac{\partial \omega}{\partial x} + V_{2a}\frac{\partial \omega}{\partial \theta} = 0.$$

The perturbation streamfunction can be decomposed into homogenous and particular components $\Psi = \Psi_h + \Psi_p$, such that

$$\nabla^2 \Psi_h = 0, \quad \text{and} \quad -\nabla^2 \Psi_p = \omega.$$

16

The general solution for the homogenous component can easily be shown to be

$$\Psi_h(x,\theta,t) = B_k(t)\exp(kx + ik\theta) + C_k(t)\exp(-kx + ik\theta).$$

An approximation for the particular solution follows.

The vorticity convection equation has the solution

$$\omega(x,\theta,t) = \omega\left(t - \frac{x}{\Phi_{2a}}, \theta - \frac{V_{2a}x}{\Phi_{2a}}\right).$$

If harmonic dependence on θ is required and if $\omega_{0,k}(t)$ is defined such that

$$\omega(0,\theta,t) = \omega_{0,k}(t)\exp(ik\theta),$$

then

$$\omega(x,\theta,t) = \omega_{0,k}\left(t - \frac{x}{\Phi_{2a}}\right)\exp\left[ik\left(\theta - \frac{V_{2a}x}{\Phi_{2a}}\right)\right].$$

The convective delay will be approximated by a lag equation. If ω_0 and ω_x are defined such that

$$\omega_0(t) = \omega(0,\theta,t) \quad \text{and} \quad \omega_x(t) = \omega(x,\theta,t),$$

then clearly $\omega_x(t + \tau) = \omega_0(t)$, where $\tau = x/\Phi$.

The Laplace transform of ω_0 is given by

$$\mathcal{L}[\omega_0(t)] = \mathcal{L}[\omega_x(t + \tau)] = e^{s\tau}\mathcal{L}[\omega_L(t)].$$

Hence,

$$\frac{\mathcal{L}(\omega_x)}{\mathcal{L}(\omega_0)} = e^{-s\tau}.$$

If the exponential is replaced by its (1-1) Pade approximation, one obtains

$$\frac{\mathcal{L}(\omega_x)}{\mathcal{L}(\omega_0)} = \frac{2 - s\tau}{2 + s\tau} = -1 + \frac{4}{2 + s\tau}.$$

Introducing $h(t)$ such that

$$\mathcal{L}(h) = \frac{4\mathcal{L}(\omega_0)}{2 + s\tau},$$

yields the two equations:

$$(2 + s\tau)\mathcal{L}(h) = 4\mathcal{L}(\omega_0),$$
$$\mathcal{L}(\omega_x) = -\mathcal{L}(\omega_0) + \mathcal{L}(h).$$

Applying the inverse Laplace transformation, one may solve for ω_x in terms of ω_0 and h,

$$\omega_x(t) = h(t) - \omega_0(t)$$
$$\frac{dh}{dt} = \frac{2}{\tau}(-h + 2\omega_0).$$

17

Thus for $x > 0$,

$$\omega(x, \theta, t) \approx [h_k(x, t) - \omega_{0,k}(t)] \exp(ik\theta - ikVx/\Phi),$$

$$\frac{\partial h_k}{\partial t} = \frac{2\Phi_{2a}}{x}(-h_k + 2\omega_{0,k}). \tag{13}$$

Finally, the dependence of the vorticity on x must be considered. If the vorticity is assumed to vary linearly with x,

$$
\begin{aligned}
\omega(x, \theta, t) &= \left(1 - \frac{x}{L}\right)\omega(0, \theta, t) + \frac{x}{L}\omega(L, \theta, t) \\
&= \left(1 - \frac{x}{L}\right)\omega_{0,k}(t)\exp(ik\theta) + \frac{x}{L}[h_k(t) - \omega_{0,k}(t)]\exp(ik\theta - ikVL/\Phi),
\end{aligned}
$$

where

$$\frac{dh_k}{dt} = \frac{2\Phi}{L}(-h_k + 2\omega_{0,k}),$$

then the particular component of the streamfunction must also vary linearly with x, hence,

$$
\begin{aligned}
\Psi_p(x, \theta, t) &= \int\int \omega(x, \theta, t)d\theta d\theta, \\
&= \frac{1}{k^2}\left\{\left(1 - \frac{x}{L}\right)\omega_{0,k}(t)\exp(ik\theta)\right. \\
&\qquad \left. + \frac{x}{L}[h_k(t) - \omega_{0,k}(t)]\exp(ik\theta + ikVL/\Phi)\right\}.
\end{aligned}
$$

The boundary conditions at the upstream end of the inter-blade space together with equation 13 relate the constants defining the streamfunction, $B_k(t)$, $C_k(t)$, $\omega_{0,k}(t)$, and $h_k(t)$ to the perturbation quantities $\phi_{2a}(\theta, t)$, $v_{2a}(\theta, t)$, $p_{2a}(\theta, t)$ and the nominal velocity components Φ_{2a} and V_{2a}:

$$\phi_{2a}(\theta, t) = \left. +\frac{\partial \Psi}{\partial \theta}\right|_{x=0} \tag{14}$$

$$v_{2a}(\theta, t) = \left. -\frac{\partial \Psi}{\partial x}\right|_{x=0} \tag{15}$$

$$\frac{\partial p_{2a}}{\partial \theta} = \left.\left[\frac{\partial^2 \Psi}{\partial x \partial t} + \Phi\frac{\partial^2 \Psi}{\partial x^2} + V\frac{\partial^2 \Psi}{\partial x \partial \theta}\right]\right|_{x=0}. \tag{16}$$

Likewise, the boundary conditions at the downstream end relate the perturbation quantities $\phi_{2b}(\theta, t)$, $v_{2b}(\theta, t)$, $p_{2b}(\theta, t)$ to the constants defining the streamfunction $B_k(t)$, $C_k(t)$, $\omega_{0,k}(t)$, $h_k(t)$, and Φ_{2a} and V_{2a},

$$\phi_{2b}(\theta, t) = \left. +\frac{\partial \Psi}{\partial \theta}\right|_{x=\text{ibs}} \tag{17}$$

18

$$v_{2b}(\theta, t) \quad = \quad -\left.\frac{\partial\Psi}{\partial x}\right|_{x=\text{ib}_\bullet} \tag{18}$$

$$\frac{\partial p_{2b}}{\partial\theta} \quad = \quad \left[\frac{\partial^2\Psi}{\partial x\partial t} + \Phi\frac{\partial^2\Psi}{\partial x^2} + V\frac{\partial^2\Psi}{\partial x\partial\theta}\right]\Bigg|_{x=L_{\text{ib}_\bullet}}. \tag{19}$$

2.8   Actuation by bleed of mass flow

The bleeding of mass flow is a physically-realizable means of control. Bleed is incorporated into the present reduced-order model through an actuator disk just downstream from the inter-bladerow space. As one would expect, the efficacy of control is strongly dependent on the axial position of the bleed valve.

The actuator disk matching conditions are found from the balance of mass and momentum flow through the control volume sketched in figure (5). The
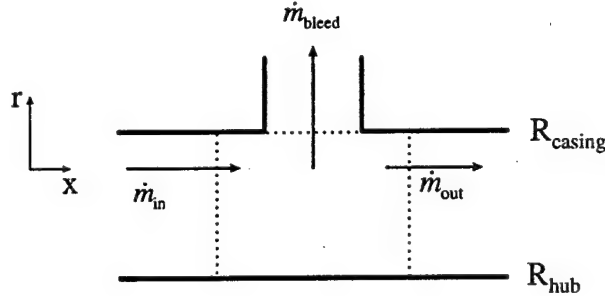

Figure 5: Sketch of bleed control volume.

axial dimension of the control volume is taken to be sufficiently small that the instantaneous mass and momentum within may be neglected. The mass flow equation is

$$\dot{m}_{\text{in}} - \dot{m}_{\text{bleed}} - \dot{m}_{\text{out}} = 0,$$

the equation for the flow of axial momentum is

$$P_{\text{in}}A - P_{\text{out}}A \quad = \quad \frac{d}{dt}(mu)$$

19

$$= \dot{m}_{\text{in}} u_{\text{in}} - \dot{m}_{\text{bleed}} u_{\text{bleed}} - \dot{m}_{\text{out}} u_{\text{out}},$$

and the equation for the flow of tangential momentum is likewise

$$0 = \frac{d}{dt}(mv)$$
$$= \dot{m}_{\text{in}} v_{\text{in}} - \dot{m}_{\text{bleed}} v_{\text{bleed}} - \dot{m}_{\text{out}} v_{\text{out}}.$$

As an additional constraint, it is assumed that $u_{\text{bleed}} = u_{\text{in}}$ and $v_{\text{bleed}} = v_{\text{in}}$. The axial dimension of the control volume is assumed to sufficiently small that the instantaneous mass within can be neglected.

The nondimensional equations for the bleed actuator disk are found to be

$$\phi_{2b} - \xi - \phi_{2c} = 0 \tag{20}$$
$$p_{2b} - p_{2c} - \xi\phi_{2b} + \xi^2 = 0 \tag{21}$$
$$v_{2b} - v_{2c} = 0, \tag{22}$$

where all quantities depend on θ and t.

2.9   Conservation equations for the stator

The stator is modeled as a rigid blade row. Matching conditions for the actuator disk are given by conservation of mass, the Bernoulli equation with the inclusion of a loss term. Further it is assumed that the exit angle of the flow is fixed by the metal angle of the blade (which is taken to be zero). Conservation of mass can be expressed

$$\phi_{2c} = \phi_3; \tag{23}$$

the Bernoulli equation for the flow across the stator is

$$\left(p_{2c} + \frac{\phi_{2c}^2 + v_{2c}^2}{2} - L_{\text{s}} \right) - \left(p_3 + \frac{\phi_3^2}{2} \right) = \frac{c_{\text{s}}}{\cos\gamma_{\text{s}}} \frac{d\phi_{2c}}{dt}, \tag{24}$$

where L_{s} represents a loss in leading-edge total pressure and v_3 is fixed to be zero.

2.10   Lagged-loss equations

The total pressure losses across the rotor and stator actuator disks are assumed to lag their quasi-static values. A simple one-dimensional lag equation is used in each case,

$$\tau_{\text{r}} \left(\frac{\partial}{\partial t} - \frac{\partial}{\partial \theta} \right) L_{\text{r}} = -(L_{\text{r}} - L_{\text{r,qs}}), \tag{25}$$

and

$$\tau_{\text{s}} \frac{\partial L_{\text{s}}}{\partial t} = -(L_{\text{s}} - L_{\text{s,qs}}). \tag{26}$$

20

The quasi-static losses are taken to be functions of incidence angle,

$$\begin{aligned}
L_{r,qs} &= L_{r1}\alpha_{inc,r}^2 + L_{r2}\alpha_{inc,r} + L_{r3} \\
L_{s,qs} &= L_{s1}\alpha_{inc,s}^2 + L_{s2}\alpha_{inc,s} + L_{s3},
\end{aligned}$$

where

$$\alpha_{inc,s} = -\tan^{-1}\left(\frac{v_{2c}}{\phi_{2c}}\right) - \beta_{zs}.$$

$\alpha_{inc,r}$ is defined in section 2.2.

2.11 Exit duct

The flow in the exit duct is assumed to be incompressible and rotational. It is assumed that the stator fixes the exit flow angle to zero and the length of the duct is assumed infinite. The more general case of nonzero exit flow angle is treated in reference [4].

To first order, the pressure perturbation satisfies a Poisson equation,

$$\nabla^2 p = 0,$$

which yields solutions of the form

$$p = p_{3n}(t)e^{-nx}e^{in\theta}.$$

The assumption of an infinite duct precludes the possibility of upstream propagating waves. The flow must also satisfy the linearized axial momentum and continuity equations,

$$\frac{\partial\phi}{\partial t} + \Phi\frac{\partial\phi}{\partial x} + V\frac{\partial\phi}{\partial\theta} = -\nabla p,$$

and

$$\frac{\partial\phi}{\partial x} + \frac{\partial v}{\partial\theta} = 0.$$

At the exit face of the stator ($x = 0$) the flow angle is assumed to be zero, thus,

$$V = \frac{\partial v}{\partial\theta} = 0.$$

Continuity requires then

$$\frac{\partial\phi}{\partial x} = 0,$$

at $x = 0$, thus the axial momentum equation reduces to

$$\dot{\phi}_{3n} = np_{3n}. \tag{27}$$

As in the inlet, the axisymmetric variables are assumed to be related through a momentum equation through a finite-length, uniform duct. Following Moore

and Greitzer [6], the exit duct is assumed to empty into a plenum. From the plenum, flow exits through an orifice back into the constant total pressure reservoir. Moore and Greitzer were motivated by the stability of compressors for which it is reasonable to assume a complete loss of dynamic head when the flow dumps into the plenum. The present analysis is motivated by the bypass flow of a large turbofan engine. In this case the exit duct simply discharges into the atmosphere.

The equation for momentum conservation in the duct is taken to be

$$(P_3 + \frac{1}{2}\Phi_3^2) - (P_\text{p} + \frac{1}{2}C_d\Phi_3^2) = L_\text{exit}\dot{\Phi}_3. \tag{28}$$

As a generalization of the surge modeling of Moore and Greitzer, C_d is introduced as a coefficient modifying the loss of dynamic head. The extreme cases are given by $C_d = 1$ in which all dynamic head is lost as the duct dumps into the plenum and by $C_d = 0$ in which the flow passes without loss through a diffuser.

The equation for mass conservation within the plenum may be expressed

$$4B^2 L_c \dot{P}_\text{p} = \Phi_3 - A\sqrt{2(P_\text{p} - P_\text{atm})}, \tag{29}$$

following Moore and Greitzer. Greitzer's B parameter is proportional to the square root of the volume of the plenum. The bypass flow of a turbofan is best modeled by the combination

$$C_d = B = 0.$$

3 Model reduction

Each system variable is projected over a finite number of Fourier components in the azimuthal variable. For example,

$$\phi_1(\theta, t) = \phi_{1,1}(t) + \sum_{n=1}^{N} \phi_{1,2n} \cos n\theta - \phi_{1,2n+1} \sin n\theta.$$

Thus, in equation 3,

$$\Phi_1(t) = \phi_{1,1}(t),$$

and in 1

$$\phi_{1n}(t) = \phi_{1,2n}(t) + i\phi_{1,2n+1}(t).$$

A time-dependent system of equations is derived through a Galerkin projection of equations 1 — 29 over the Fourier modes. Equations 3,10,11,12,28, and 29 relate the nominal axisymmetric flow quantities and are already functions of time alone. Equations 1, 2, 13, 14, 15, 16, 17, 18, 19, and 27 relate the flow perturbations only and need must be projected over the basis $\{\cos n\theta, \sin n\theta\}$, for $n = 1 \ldots N$. Finally, equations 4, 5, 6, 7, 8, 9, 20, 21, 22, 23, 24, 25, and 26 involve axisymmetric and perturbation terms and thus must be projected over the basis $\{1, \cos n\theta, \sin n\theta\}$, for $n = 1 \ldots N$. Equations 8 and 9 are second-order in time, and equation 6 is a vector equation with two components. Written as a system of first order differential-algebraic equations,

$$f(x, \dot{x}, p) = 0,$$

the total number of equations and state variables is $52N + 22$.

4 Linear stability analysis

Linear stability is a key element in determining the bounds on the parameter space for design and operation of the turbomachine. It is feasible using the reduced-order model to quickly determine system damping and qualitatively-accurate boundaries to linear stability as the system parameters are varied. This will be the primary tool for predicting the system operability map, determining the sensitivity of flutter instability to installation effects, viscosity (losses and deviation), and mistuning, and investigating system identification and control.

The reduced-order model is expressed as an autonomous system of differential-algebraic equations

$$\Delta(x, \dot{x}, p) = 0, \tag{30}$$

where x is the state vector and p is a vector of parameters. The fixed points $\overline{x}_p$ of system (30) satisfy the nonlinear algebraic system

$$\Delta(\overline{x}, 0, p) = 0,$$

which may be solved iteratively. The locus of fixed points as the throttle is varied at constant shaft speed correspond to a characteristic or speedline of the turbomachine. Typically plotted as pressure rise versus mass flow, the characteristic has a peak at which the maximum possible pressure rise is achieved.

The stability of each point on the speedline may be determined from the generalized eigenvalue problem

$$[\lambda \Delta_{\dot{x}} + \Delta_x] x = 0, \tag{31}$$

where

$$\Delta_{\dot{x}} = \left. \frac{\partial \Delta}{\partial \dot{x}} \right|_{\overline{x}} \quad \text{and} \quad \Delta_x = \left. \frac{\partial \Delta}{\partial x} \right|_{\overline{x},}$$

the linearization of system (30) about the fixed point $\overline{x}$. The eigenvalue problem (31) is solved numerically using the RGG routine of the SLATEC (EISPACK) subroutine library [7]. The eigenvalues λ are returned as a ratio

$$\lambda = \alpha/\beta,$$

where α is complex and β is real. The matrix $\Delta_{\dot{x}}$ is typically singular, hence, only the eigenvalues for which β is nonzero are relevant to system stability.

The relative stability of a system eigenmode is concisely described by its damping ratio. If the eigenvalue is given by

$$\lambda = \alpha + i\omega,$$

the damping ratio is

$$\zeta = -\frac{\alpha}{\sqrt{\omega^2 + \alpha^2}}.$$

24

$\zeta < 0$ indicates the mode is unstable. The damping of flutter modes is computed with respect to the blade-fixed coordinates, hence

$$\zeta = -\frac{\alpha}{\sqrt{(\omega^2 - in) + \alpha^2}},$$

where n is the Fourier nodal diameter of the flutter mode (positive or negative).

5 System stability

The parameters governing operation are the throttle parameter, the shaft speed (by which time is nondimensionalized), and the inlet total pressure. At constant altitude operation, such as in a test facility, it is reasonable to fix the inlet total pressure to a constant value. The locus of equilibria as the throttle is varied at constant shaft speed is referred to as a speedline. It is often plotted as total-to-static pressure rise against the flow coefficient. The operating line or "op line" is the locus of equilibria as the shaft speed is varied at a particular value of the throttle parameter. In this section, the dependence of system stability on throttle and shaft speed is considered. All other parameters are assigned nominal values consistent with a small-scale research rig. These are given in table 3. The dependence of system stability on blade geometry, duct lengths, and other parameters is considered elsewhere.

The fundamental system instabilities are high-incidence flutter and rotating stall. These occur as circumferentially travelling waves. Flutter can be either forward or backward travelling. Stall is always a forward travelling wave. Due to axial symmetry, the instability modes decouple into their Fourier harmonics, or nodal diameter patterns. For large values of the Greitzer-B parameter surge is also a fundamental instability. The flutter eigenvalues lie very near their natural frequencies i$(\omega_b \pm n)$ and i$(\omega_t \pm n)$ consistent with the understanding that the aeroloading is small in comparison to the elastic restoring forces.

Neglecting structural damping and aero-loading in the (rotor frame) blade deflection equations 8 and 9, yields the following conservative system:

$$\ddot{q} + (\xi_{ea} - \xi_{cg})c\ddot{\alpha} + Q_b^2 q = 0,$$

$$\ddot{\alpha} + \frac{(\xi_{ea} - \xi_{cg})cD}{I_{ea}}\ddot{q} + Q_t^2 \alpha = 0.$$

Except for the case in which the elastic axis and center of gravity are coincident, each of the two mode shapes involves coupled bending and twist. Assuming harmonic response, it is easily shown that the natural frequencies of the flutter modes are given by

$$\begin{aligned}
\omega_b^2 &= \frac{Q_t^2 + Q_b^2 - \sqrt{(Q_t^2 - Q_b^2)^2 + 4\mu Q_b^2 Q_t^2}}{2(1 - \mu)}, \\
\omega_t^2 &= \frac{Q_t^2 + Q_b^2 + \sqrt{(Q_t^2 - Q_b^2)^2 + 4\mu Q_b^2 Q_t^2}}{2(1 - \mu)},
\end{aligned} \qquad (32)$$

where

$$\mu = \frac{(\xi_{ea} - \xi_{cg})^2}{(\xi_{ea} - \xi_{cg})^2 + \epsilon^2}$$

and it is assumed that $\omega_b < \omega_t$. In the limit $\mu \to 0$, $\omega_b = Q_b$ and $\omega_t = Q_t$.

Table 3: Nominal values for system parameters.

P_{atm}	$= 2.17 \times 10^6 \, \mathrm{s}^{-2}/\Omega^2_{\mathrm{shaft}}$	atmospheric pressure.
$c_{\mathrm{s}}/\cos(\gamma_{\mathrm{s}})$	$= 0.2086,$	effective length of stator blade passage.
β_{r}	$= 15°,$	trailing edge metal angle of rotor,
β_{zr}	$= 45°,$	zero-incidence angle of rotor leading edge,
β_{zs}	$= 32°,$	zero-incidence angle of stator leading edge,
B	$= 0,$	Greitzer-B parameter (surge).
C_d	$= 0,$	plenum loss coefficient.
N_b	$= 16,$	number of blades
c_{r}	$= 0.4560,$	rotor chord.
D	$= 14.6,$	blade mass.
γ_r	$= 30°,$	stagger angle.
α_{inlet}	$= 0.5,$	inlet geometry parameter.
L_{inlet}	$= 0.5,$	actual length of inlet duct.
L_{exit}	$= 0.5,$	actual length of exit duct.
τ_{r}	$= 0.61,$	time scale for rotor loss.
τ_{s}	$= 0.32,$	time scale for stator loss.
Δ_1	$= 0.18,$	coefficient of the empirical rotor deviation function.
Δ_2	$= 12°,$	coefficient of the empirical rotor deviation function.
L_{ibs}	$= 0.3,$	length of inter-bladerow space.
ξ_{cg}	$= 0.35,$	position of the center of gravity divided by chord.
ξ_{cp}	$= 0.35,$	position of the center of pressure divided by chord.
L_{r1}	$= 1.8842,$	coefficients of the empirical rotor loss function.
L_{r2}	$= -0.5053,$	
L_{r3}	$= 0.1219,$	
L_{s1}	$= 0.7429,$	coefficients of the empirical stator loss function.
L_{s2}	$= -0.1450,$	
L_{s3}	$= 0.0951.$	
ξ_{ea}	$= 0.55,$	position of the elastic axis divided by chord.
ϵ	$= 0.20,$	rotational inertia divided by chord.
Q_b	$= 2620 \, \mathrm{s}^{-1}/\Omega_{\mathrm{shaft}},$	frequency of pure bending (nondimensionalized by Ω_{shaft}).
Q_t	$= 1990 \, \mathrm{s}^{-1}/\Omega_{\mathrm{shaft}},$	frequency of pure twist (nondimensionalized by Ω_{shaft}).
ζ_b	$= 0.035,$	structural damping of bending mode.
ζ_t	$= 0.035,$	structural damping of torsion mode.

Solution of the fixed point problem and generalized eigensystem analysis are sufficient to determine system stability but not system operability because rotating stall typically occurs as a subcritical Hopf bifurcation, hence there is a region of parameter space in which the system equilibrium is locally stable but globally unstable.

In figure (6) is plotted a speedline for $\Omega_{shaft} = 942\,s^{-1}$ (9000 RPM). The fixed point value of plenum pressure is plotted against the fixed point value of flow coefficient the throttle parameter is varied. The fixed points of system 30 are computed using Newton-Raphson iteration. The points of flutter and stall instability are indicated. Stall instability typically occurs near the peak of the total-to-static pressure rise. If it is assumed that the compression system operates in a quasi-steady manner such that the pressure rise is a function of flow coefficient only, it can be shown that instability always occurs at the peak. In reality, compression systems have a finite response time and it has been shown that this has a stabilizing effect [3].

Loci of stator-frame eigenvalues corresponding to the speedline of figure (6) are plotted in figure (7). For clarity, only a subset of the least stable modes is shown. The flutter and stall frequencies are nearly constant over the speedline. The growth rates (determined by real part) are very different however; in comparison to the flutter eigenvalues, the stall eigenvalue moves much faster from very stable to instability over the speedline. The variation of blade-frame damping ratio along the speedline for the lowest nodal diameter mode-1 flutter modes is plotted in figure (8). At a fixed point on the speedline, the damping of the mode 1 flutter modes is plotted in figure (9). The current configuration has eight blades, hence the x-axis of figure (9) corresponds to a range of inter-blade phase angle from -180 to 180 degrees. The variation of stall damping ratios over the speedline is plotted in figure (10). Note that the scale over which stall damping varies is much larger than the scale over which flutter damping varies. For the chosen set of parameters, the initial instability is forward-travelling first nodal diameter flutter.

The operability of a engine can be characterized by its response as the mass flow rate and shaft speed are independently varied. Other important effects which are not considered here are nonuniform inlet flows, including flows with nonzero incidence and gusts. The sensitivity to inlet total pressure is considered in a later section (6.7). The stability boundaries of the least-stable modes as the throttle parameter and shaft speed are independently varied are plotted in figure 11. The region of stable operation is bounded by the zero-nodal and first forward-travelling flutter boundaries. For this set of parameters, flutter always occurs before stall. Linear stability however is not a conservative measure of operability; the stall instability is typically subcritical, thus there is a parameter space for which the operating point is locally stable but unstable to sufficiently large perturbations.

The information in the bifurcation set of figure 11 can be conveyed in terms of engine performance. Each point in the parameter set corresponds to a different
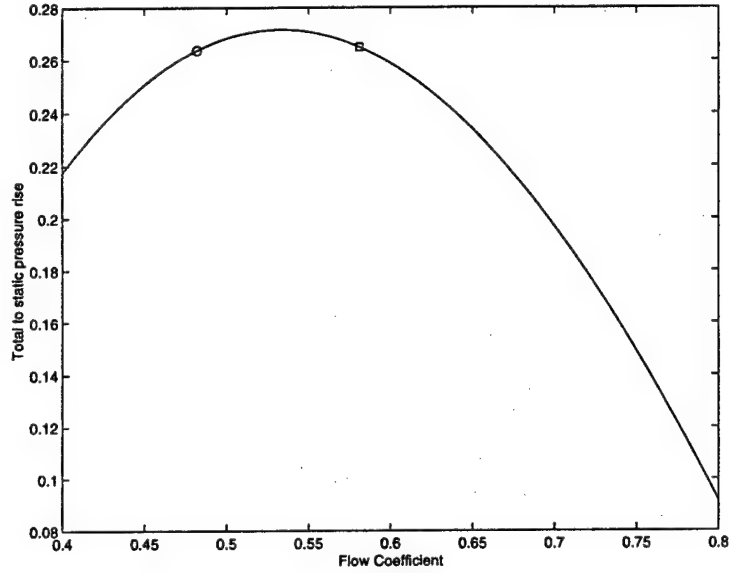
28

Figure 6: Speedline for $\Omega_{\text{shaft}} = 942\,\text{s}^{-1}$ (9000 RPM). Critical flutter mode is first nodal diameter, forward travelling ($ND1+$). Critical stall mode is also first nodal diameter. Onset of flutter and stall instabilities are indicated by □ and ○, respectively.

equilibrium point. In figure 12 are plotted the nondimensional exit pressure and flow coefficient corresponding to the stability boundaries of figure 11. In figure 13 are plotted stability boundaries in terms of the more conventional performance measures of pressure ratio and inlet Mach number. The conversions from nondimensional exit pressure and flow coefficient to pressure ratio and inlet Mach number assume engine dimensions comparable to a laboratory-scale test facility.
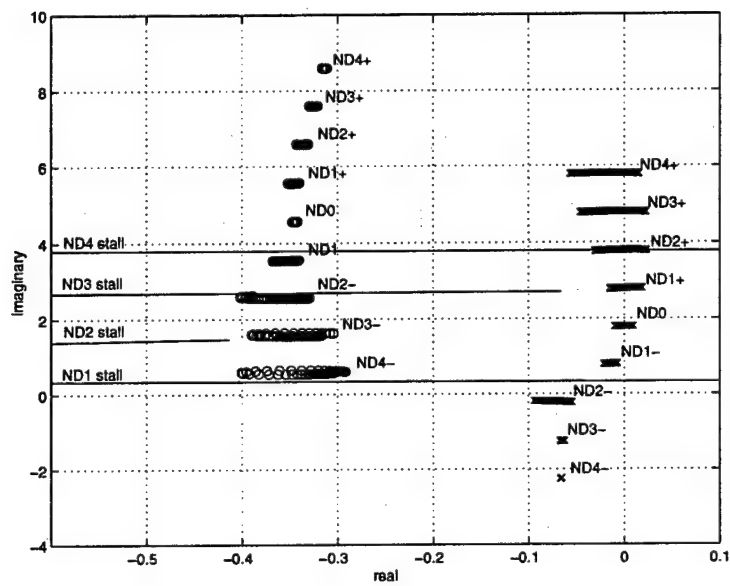
Figure 7: Root locus of least-stable eigenvalues corresponding to speedline. ×, first structural flutter mode. o, second structural flutter mode.
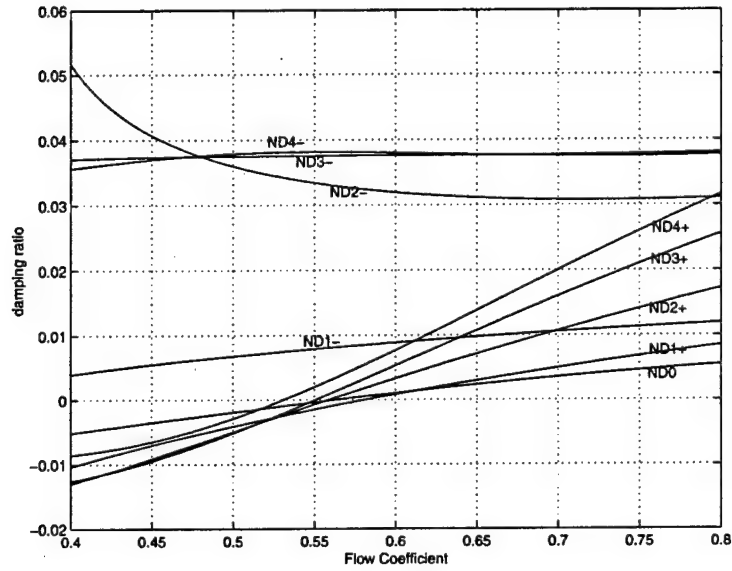
Figure 8: Variation of mode 1 flutter damping with flow coefficient.
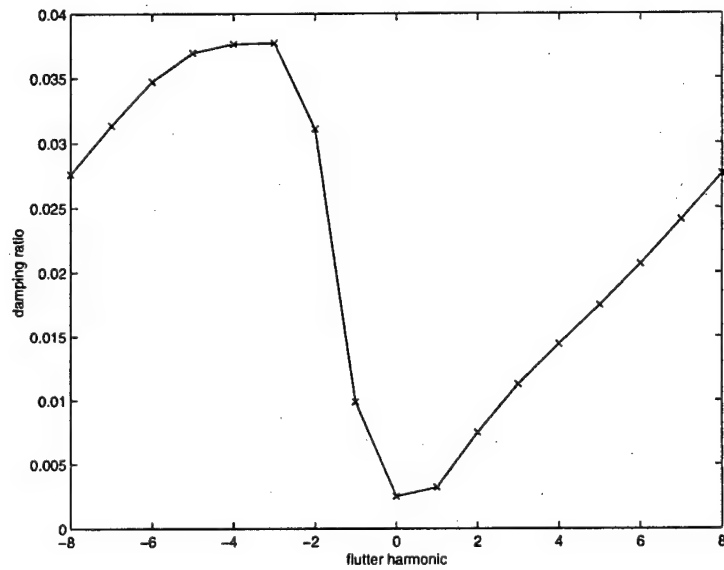
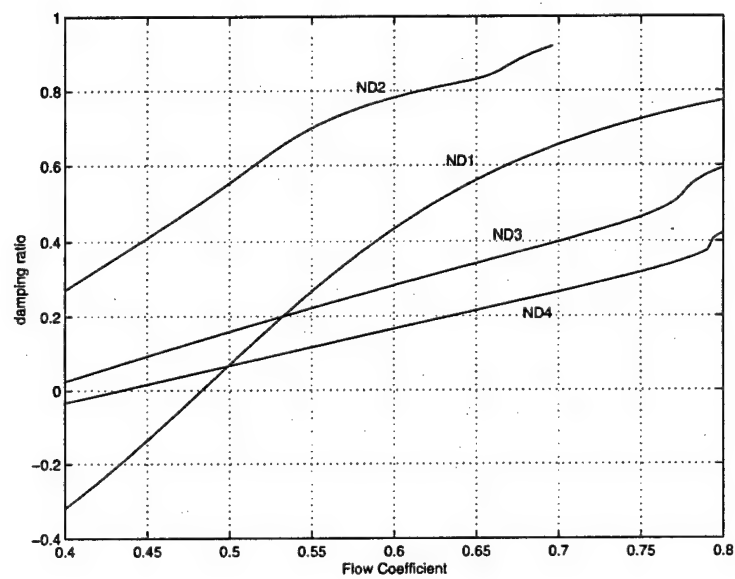Figure 9: Mode 1 flutter damping by nodal diameter, $\Phi = 0.65$, $N_b = 16$.

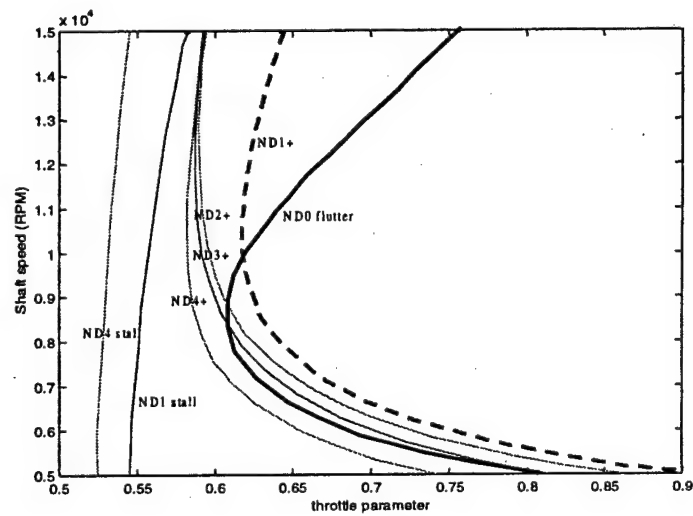Figure 10: Variation of stall damping with flow coefficient.
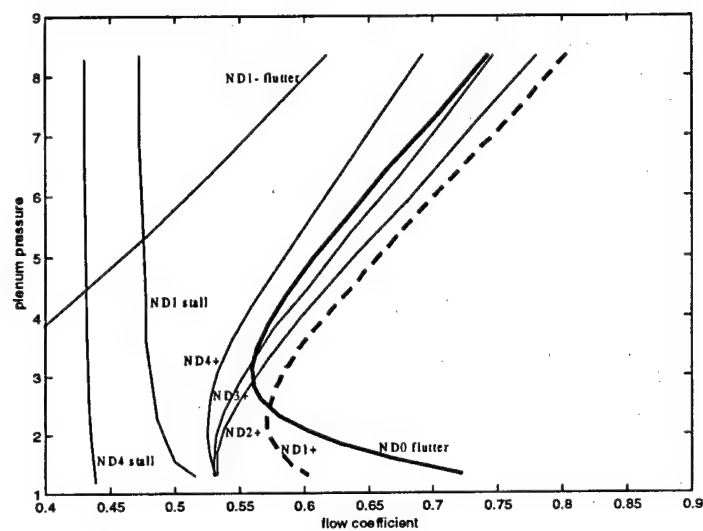
Figure 11: Two parameter bifurcation diagram. Linear stability boundaries as throttle and shaft speed are independently varied. The critical boundaries are indicated with heavy lines; — ND0 flutter boundary, – – ND1+ flutter boundary. Operation in the region to the right (higher values of throttle) of the critical stability boundaries is stable.

33

Figure 12: Stability boundaries as throttle and shaft speed are independently varied. The critical boundaries are indicated with heavy lines; — ND0 flutter boundary, - - ND1+ flutter boundary. Operation in the region to the right (higher values of flow coefficient) of the critical stability boundaries is stable.
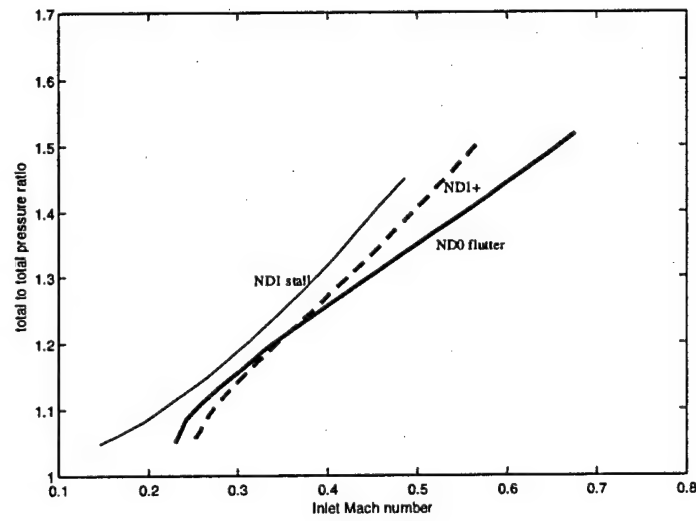
Figure 13: Stability boundaries as throttle and shaft speed are independently varied. Inlet Mach number is computed assuming $R_{\mathrm{nom}} = 23.4\,\mathrm{cm}$ and sonic velocity $c = 330\,\mathrm{m/s}$. The critical boundaries are indicated with heavy lines; — ND0 flutter boundary, – – ND1+ flutter boundary. Operation in the region to the right (higher values of inlet Mach number) of the critical stability boundaries is stable.

35

6 Parametric Sensitivity

The sensitivity of system stability to parameter variations is examined by computing partial derivatives of the damping ratios of several flutter and stall modes with respect to system parameters (table 2). A point on the speedline $\Phi = 0.55$ near the peak pressure rise is taken as the reference. Nine flutter modes were examined, zero nodal diameter, and the first four nodal diameters, forward and backward travelling modes. The first four stall modes were examined. The parametric sensitivity will vary of course with the choice of equilibrium and nominal parameter values.

The sensitivity of first nodal diameter, forward travelling flutter damping to parameter variations is indicated in figure 14. The other flutter modes show greatest sensitivity to the same parameter set although in varying degree and sense (positive or negative). Not surprisingly flutter damping was found to be most strongly influenced by the structural damping parameters, ζ_t and ζ_t. Structural damping is stabilizing to all of the flutter modes. Next in order of importance are the parameters which govern the natural frequencies and the plunge to twist ratios, ξ_{ea}, ξ_{cg}, ϵ, Q_t and Q_b. Also important is the center of pressure offset parameter ξ_{cp} which strongly affects the gain (section 2.6). In contrast, the chord and blade inertia parameters c_r and D affect the gain only weakly. As discussed in section 5 flutter damping increases with throttle parameter A. Flutter damping is shown to be sensitive to the orientation and shape of both rotor and stator as well as the loss and deviation.

The sensitivity of first nodal diameter stall damping to parameter variations is indicated in figure 15. The other stall modes are sensitive to the same parameters and for some of the parameters the sense of the dependence is uniform. As expected, the damping of the stall modes is most sensitive to those parameters which determine the steady characteristic and to the throttle parameter. For these parameters, variations are either stabilizing for all modes, or de-stabilizing for all modes. For other parameters which strongly influence stall damping, variations may be either stabilizing or destabilizing depending on the stall mode. These parameters include the lagged loss parameters τ_r and τ_s, the parameters which determine the inertia of fluid within the blade passages $c_s / \cos \gamma_s$ and c_r, the parameters which determine the inertia of fluid in the ducts α_{inlet} and L_{ibs}, and the parameters which determine the plunge to twist ratio and frequency.

6.1 Sensitivity of flutter to ratio of plunge to twist.

Apart from the structural damping parameters, which directly affect flutter damping, the most influential parameters to flutter damping are those which govern the plunge to twist ratio of blade deformation its natural frequencies. Since aero-loading and structural damping are small, the frequencies and plunge to twist ratios are determined primarily by the conservative form of the blade deflection equations.
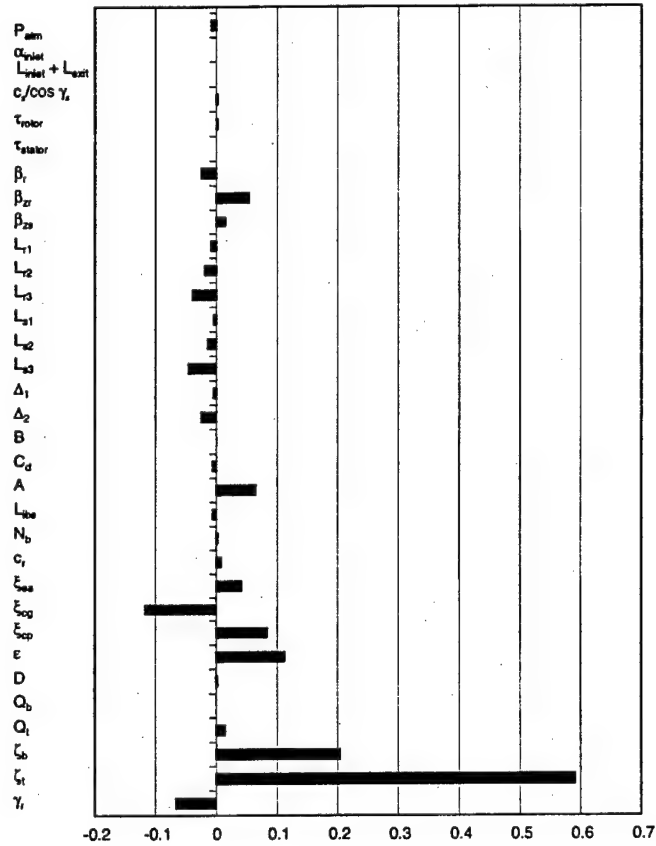
36

Figure 14: Parametric sensitivity of ND1+ flutter damping. Values plotted are partial derivatives of the damping ratio with respect to the indicated parameter.

The ratios of plunge to twist corresponding to the natural frequencies ω_b and ω_t (equation 32) are given by

$$\frac{q}{c\alpha}\bigg|_b = \frac{(\xi_{ea} - \xi_{cg})DQ_b^2}{I_{ea}[\omega_b^2(1-\mu) - Q_t^2]}$$

37

Figure 15: Parametric sensitivity of ND1 stall damping. Values plotted are partial derivatives of the damping ratio with respect to the indicated parameter.

and
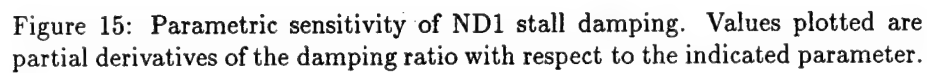
$$\left.\frac{q}{c\alpha}\right|_t = \frac{(\xi_{\mathrm{ea}} - \xi_{\mathrm{cg}})DQ_b^2}{I_{\mathrm{ea}}[\omega_t^2(1-\mu) - Q_t^2]},$$

respectively.

The sensitivity of the relative stability of the flutter modes to the plunge-to-twist ratio is illustrated in figure 16 for a small value of μ and figure 17 for

a value of μ near its upper limit. Parameters Q_b and Q_t are adjusted so that the natural frequencies remain equal to their nominal values. The highest nodal diameter patterns are found to be the least stable for large positive values of the plunge-to-twist ratio. As the ratio is decreased, the critical nodal diameter pattern decreases to the zero flutter harmonic. The interblade phase angle σ is related to the flutter harmonic number n by

$$\sigma = \frac{2\pi n}{N_b}.$$

In the present case $N_b = 16$, hence figures 16 and 17 range in interblade phase angle from -180 to 180 degrees. The two figures are qualitatively identical indicating that μ has little influence on the relative stability of the flutter modes.
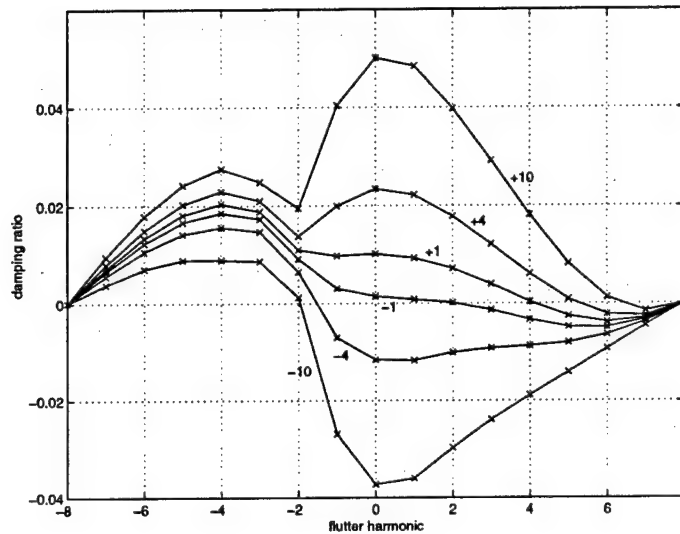
Figure 16: Relative stability of the flutter modes as the ratio of the plunge to twist is varied for μ small. The numbers by each curve indicates the value of $q/c\alpha$, the plunge to twist ratio. $\mu/\mu_{max} = 0.19$, $\omega_b = 1.81$, and $\omega_t = 4.60$.

It is shown in figure 18 that structural damping affects all of the flutter modes uniformly. The relative damping between the modes is unchanged.

6.2 Sensitivity of stability to slope of the speedline

Stall and surge instability are always found to be near the peak of the total to static pressure rise. Gysling [4] developed the argument that instability
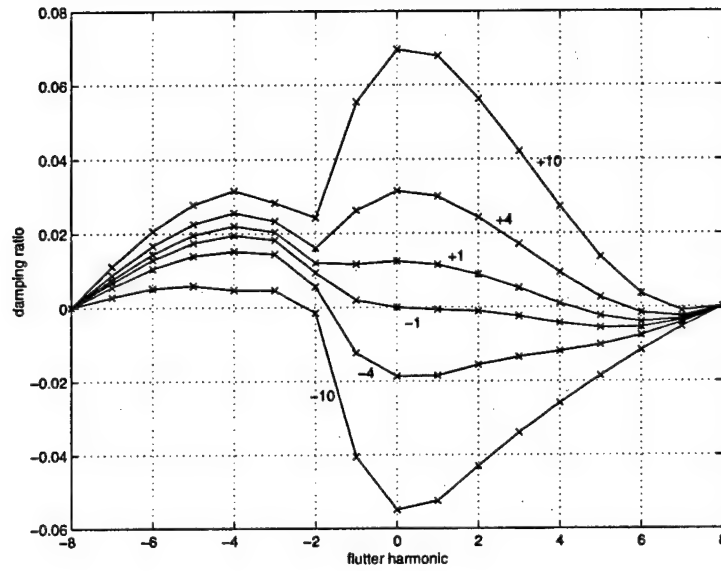
Figure 17: Relative stability of the flutter modes as the ratio of the plunge to twist is varied for μ large. The numbers by each curve indicates the value of $q/c\alpha$, the plunge to twist ratio. $\mu/\mu_{\max} = 0.93$, $\omega_b = 1.81$, and $\omega_t = 4.60$.
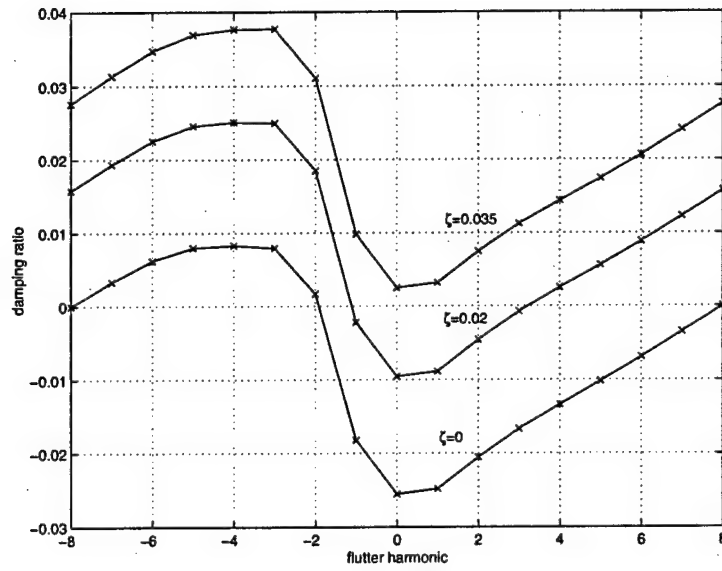
40

Figure 18: Influence of structural damping on flutter stability. Both structural damping parameters are adjusted concurrently, $\zeta_b = \zeta_t = \zeta$. The measured values of rotor-frame frequency are taken to be $\omega_b = 1.81$, and $\omega_t = 4.60$ and $\mu/\mu_{\max} = 0.93$.

occurs when mechanical energy is introduced into the flow faster than it can be convected away. The mechanical energy introduced into the flow is proportional to the total to total pressure rise,

$$\Psi_{tt} = \left(P_{out} + \frac{\Phi^2}{2}\right) - \left(P_{in} + \frac{\Phi^2 + V_{in}^2}{2}\right),$$

assuming an exit flow angle of zero. Conservation of mass requires that

$$\Phi_{in} = \Phi_{out} = \Phi.$$

The kinetic energy of the flow can be convected downstream, hence the energy balance is unstable to perturbations if

$$\partial \Psi_{tt} \geq \partial \left(\frac{\Phi^2}{2}\right),$$

or

$$\frac{d\Psi_{tt}}{d\Phi} \geq \Phi.$$

The instability criterion may be re-written

$$\frac{d\Psi_{ts}}{d\Phi} \geq 0,$$

since the total to total pressure rise is related to the total to static pressure rise by

$$\Psi_{tt} = \Psi_{ts} + \frac{\Phi^2}{2}.$$

High-incidence flutter instability is also typically found near the peak of the compressor characteristic. Figures 14 and 15 indicate that variations in parameters which affect the steady compressor characteristic have the same effect on the stability of flutter as stall. The degree of flutter sensitivity is far less however.

Damping of the flutter modes is found to be somewhat dependent on the parameters governing loss and deviation. In figure 19 are plotted values of the flutter damping ratios for zero loss and deviation, nominal loss and deviation, and loss and deviation fifty percent greater than nominal. All other parameters are fixed at their nominal values. The relative damping between flutter modes is clearly shown to be dependent on viscous effects; the least-damped flutter mode shifts from third nodal diameter forward-travelling to the zero nodal diameter mode as losses and deviation increase. Flutter is more damped for the nominal loss and deviation than for either of the other cases. A significant implication is that inviscid computational fluid dynamics codes cannot accurately predict the onset of flutter if there is no additional empirical accounting for loss and deviation. Such codes will be most accurate at predicting flutter damping for conditions of small loss and deviation.
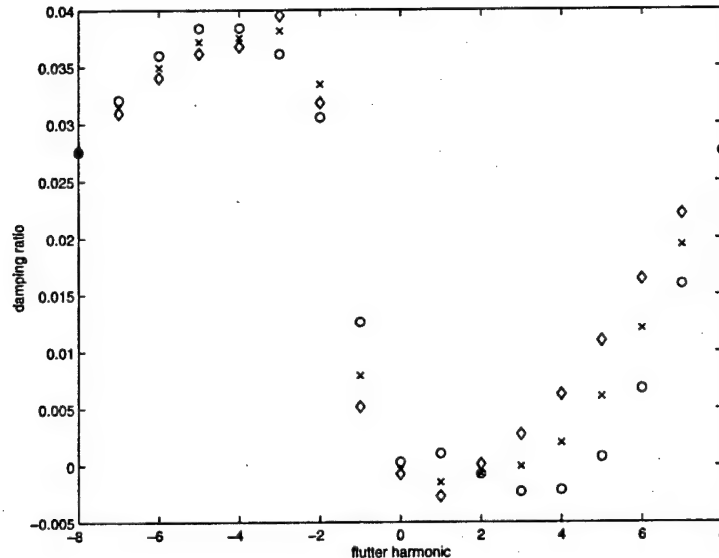
Figure 19: Sensitivity of flutter damping to loss and deviation. Damping ratios are plotted corresponding to scaling of the loss and deviation by a factors of 0 o, 1 ×, and 1.5 ⋄. The flow coefficient for these results is $\Phi = 0.55$. All other parameters take their nominal values.

If the losses are increased, the compressor peak will move right (toward higher values of flow coefficient) and the compressor will be less stable. Clearly then, increases in the loss coefficients L_{r1}, L_{r2}, L_{r3}, L_{s1}, L_{s2}, and L_{s3} destabilizes the system because the incidence angles are nearly always positive. Because the incidence angles are less than unity, L_{r3} has greater influence than L_{r2} which in turn has greater influence than L_{r1}. A similar relation holds for the stator loss coefficients. Increases in the zero-incidence angles of the blades β_{zr} and β_{zs} decreases the incidence angles (figure 4) which decreases the loss and improves compressor stability.

Increased turning of the flow results in greater pressure rise. If the pressure rise is increased the compressor peak will move towards lower values of the flow coefficient increasing system stability. This can be accomplished by decreasing the trailing-edge metal angle β_r and the flow deviation parameters Δ_1 and Δ_2.

One would suppose then that blades would be designed with large values of the zero-incidence angle and small values of the trailing-edge metal angle. This underscores the limitations of the model. In this model the loss and deviation coefficients enter as parameters which are to be identified empirically. The

43

implicit dependence on blade geometry is hidden. To a great extent, these empirical parameters are determined from the blade shape and it is known that extreme curvature of the blades can greatly increase the loss.

6.3 Sensitivity of stall to blade deflection parameters

Steady blade deformation affects the characteristic in two ways. An increase in the blade twist increases the incidence angle, and hence the loss, which is de-stabilizing. Positive blade twist also increases flow turning which is a stabilizing effect. For this set of parameters, the steady blade deflection is positive. Hence, all parameter variations which increase the steady twist will tend to affect damping in the same manner. Increases to the torsional stiffness Q_t, the center of pressure offset ξ_{cp}, and the rotational inertia ϵ all have the effect of decreasing the steady twist. For stall modes 1,3, and 4, these variations increase the damping but for mode 2, the damping is decreased (figure 20). Increases to the elastic axis offset ξ_{ea} and the center of pressure offset ξ_{cp} increase the gain of the aeroload and are found to de-stabilize modes 1,3, and 4, and stabilize mode 2.

The anomalous behavior of mode 2 can only be explained by unsteady interaction between blade deflection and flow perturbations. This is supported by the observation that the blade damping parameters have very little influence on the stability of modes 1,3, and 4 while the twist damping parameter ζ_t does have some influence on the stability of mode 2.

The parameters with greatest influence are ξ_{cp}, ξ_{cg}, and ϵ. The rotor chord c_r also is found to have a strong influence on stall damping, but the dependence is more complicated; it contributes to the gain of the aeroload and the inertia of the fluid in the blade passage.

6.4 Blade stiffness

The stiffness parameters Q_b and Q_t are not among the most influential with respect to small deviations about the nominal parameter set. As one considers very large values however, it can be shown that the flutter modes are progressively stabilized. Finally, the blades are effectively rigid and the only instability modes are stall and surge.

In figure 21 are plotted the damping ratios of the flutter modes by nodal diameter pattern for progressively higher values of the stiffness parameters. Increasing stiffness is shown to stabilize some flutter modes and to destabilize others through reduction of the aerodamping. Eventually, the aerodamping is negligible in comparison to the structural damping and all modes are equally damped.
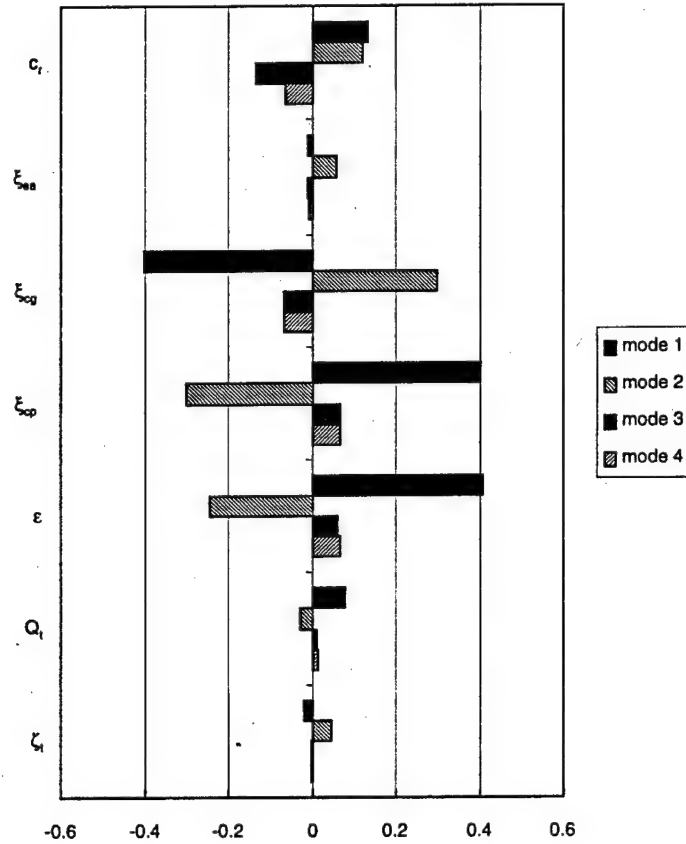
44

Figure 20: Parametric sensitivity of stall damping to parameters governing blade deflection. Values plotted are partial derivatives of the damping ratio with respect to the indicated parameter.

6.5 Unsteady loss

The effect of modeling unsteady losses with first order lag equations on stall stability has been reviewed by Longley [4]. In this section, those observations are verified for the present model and the interpretation presented by Longley is briefly re-capitulated.

The stability of the rotating stall modes is clearly affected by blade deforma-
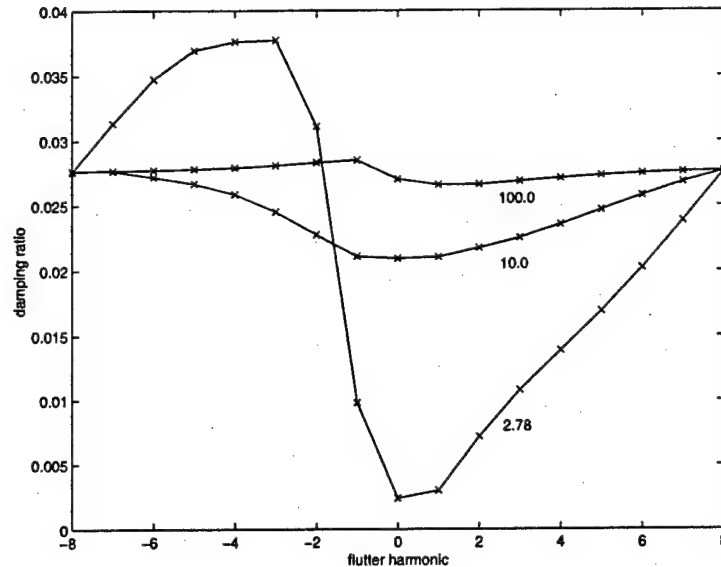
Figure 21: Relative stability of the flutter modes as the blade stiffness is varied. The numbers by each curve refer to the value of Q_b; 2.78 is its nominal value. The ratio Q_t/Q_b is held constant.

tion and by the inclusion of the inter-bladerow space. To isolate the influence of the time lags, the blade stiffness parameters are greatly increased and the length of the inter-bladerow space is greatly decreased.

For zero lag, damping of all stall modes is equal at the flow coefficient corresponding to the compressor peak as shown in figure 23. That value of damping is positive however and instability occurs in the first stall mode just beyond peak. This discrepancy is probably due to differences in the present formulation of the rotor energy equation and the unsteady Bernoulli equation which is conventional for modeling stall.

Consistent with the results presented by Longley, nonzero lag is found to be stabilizing for low flow rates, figure 25. The amount of stabilization is greater for the higher modes. At the compressor peak however, damping ratios for the first and second stall modes are actually lower than those calculated with steady losses. Comparing figures 22 and 24 it is clear that lagging of the losses results in higher frequencies than quasi-steady losses which is also consistent with Longley.

Longley has summarized earlier work demonstrating that in simplified models such as this one, lagged losses and deviation increase the effective inertia of
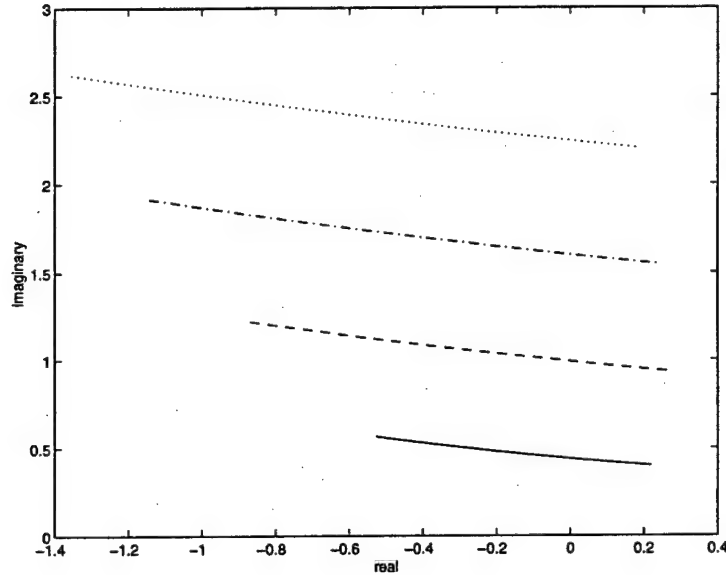
46

Figure 22: Root locus of stall eigenvalues for steady loss, short inter-bladerow space and effectively rigid blades. — 1st mode, – – 2nd mode, – · 3rd mode, · · · 4th mode. All other parameters take their nominal values.

fluid proportionately to the stall mode number within the blade passages. The argument was derived for compressors and not for fans and does not incorporate inter-bladerow flow domain. Alternatively, one may think of unsteady losses as decreasing the instantaneous slope of the compressor characteristic.

Blade deformation and the presence of the inter-bladerow gap dramatically alter the effect of unsteady losses as shown in figure 26. In contrast to the short-gap, rigid-blade case, lagged losses are shown to de-stabilize the third and fourth mode and stabilize the first and second modes. Further, the root locus of the second mode is greatly affected. In both cases however, lagging of the losses results in an increase in the stall frequency. This complicated interplay of parametric sensitivity warrants further attention. In particular, it must be verified that the Pade approximant is not introducing non-physical effects.

The effect of loss time lags on flutter stability is illustrated in figure 27. Loss time lags are shown to have a stabilizing influence on the forward-travelling waves and a destabilizing influence on the backward-travelling waves. The flutter modes are far less sensitive than are the stall modes, however the flutter modes are also lightly damped and such differences may be very significant. Certainly, this result may depend strongly on the choice of other parameters.
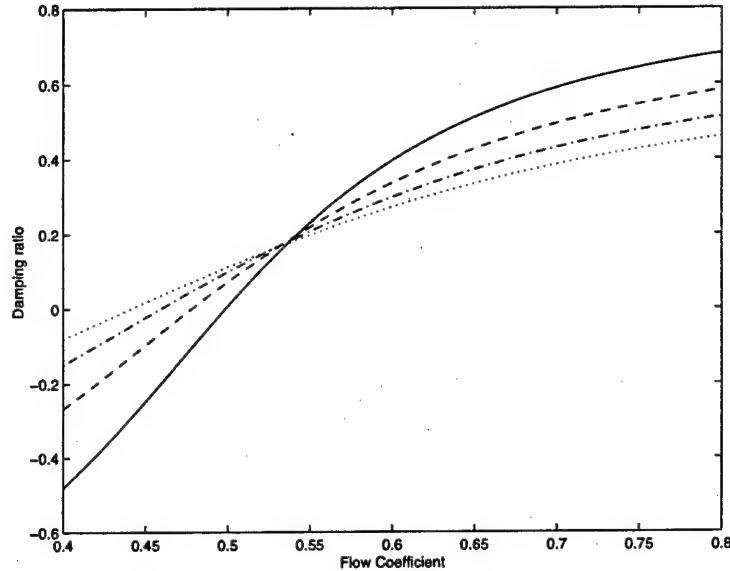
47

Figure 23: Damping ratios of stall for steady loss, short inter-bladerow space and effectively rigid blades. — 1st mode, – – 2nd mode, – · 3rd mode, · · · 4th mode. All other parameters take their nominal values.

6.6 Installation effects

The inlet geometry parameter and the length of the inter-bladerow space can effect the stability of stall and flutter modes. As discussed in section 2.1, inlet geometry clearly effects the wave numbers of the flow perturbations. Another effect of inlet geometry is that the flow velocity must be straightened as it enters the duct; a longer inlet tends to straighten the flow better upstream of the rotor face. The present model assumes nominally two-dimensional flow and cannot capture this effect. Within an inter-bladerow space it has been shown in section 2.7 that the perturbation to the flow field will have potential components (the homogenous solution) which decay exponentially from each end of the domain and a vortical component which is convected downstream. A long inter-bladerow space allows the potential perturbation to significantly decay, partially decoupling the bladerows. The effect of inter-bladerow gaps on stall instability is discussed in the review of Longley [4]. In such a case one must consider the total to static pressure rise of each bladerow. Stall instability is then found to occur when a single bladerow characteristic has zero slope and the others all have negative slope.

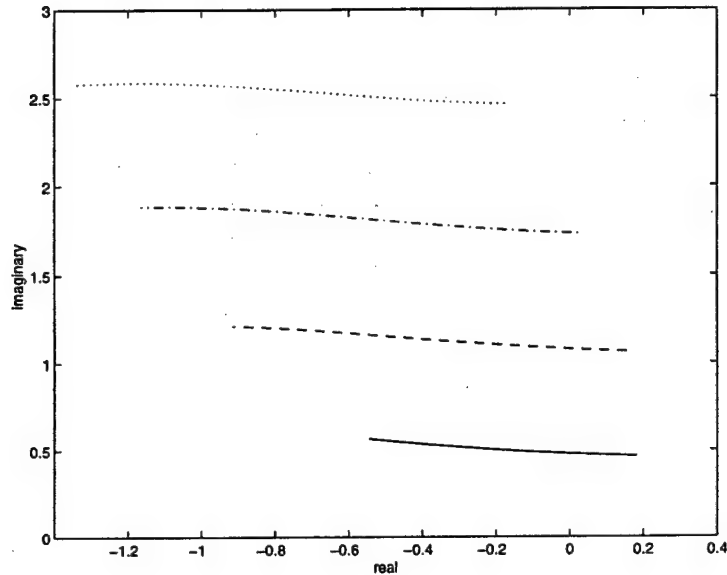The effect of the inlet geometry parameter on stall and flutter stability is

48

Figure 24: Root locus of stall eigenvalues for lagged loss, short inter-bladerow space and effectively rigid blades. — 1st mode, – – 2nd mode, – · 3rd mode, · · · 4th mode. All other parameters take their nominal values.

illustrated in figures 28 and 29. The higher-order stall modes are found to decrease in frequency and are significantly damped as the inlet parameter α_{inlet} increases from 0, an infinite inlet duct, to 2, a very short inlet duct. The first stall mode, which is the critical mode for instability, decreases in frequency but its damping ratio is nearly unchanged. The inlet parameter is shown to have no influence on flutter modes corresponding to nodal diameters 0, +8, and −8. The other forward travelling modes are found increase in damping as α_{inlet} increases (decreasing duct length); the other backward travelling waves are found to decrease in damping.

The dependence of flutter instability on the length of the inter-bladerow space is illustrated in figure 30. As in the case of inlet geometry variations, the inlet parameter is shown to have no influence on flutter modes corresponding to nodal diameters 0, +8, and −8. In contrast to the inlet duct however, long lengths of the inter-bladerow space are found to be de-stabilizing to both forward and backward-travelling modes.

The dependence of stall instability on the length of the inter-bladerow space is much more complicated. As shown in figure 31, there appear to be multiple root loci for each of the stall modes. This may be indicative that the nature
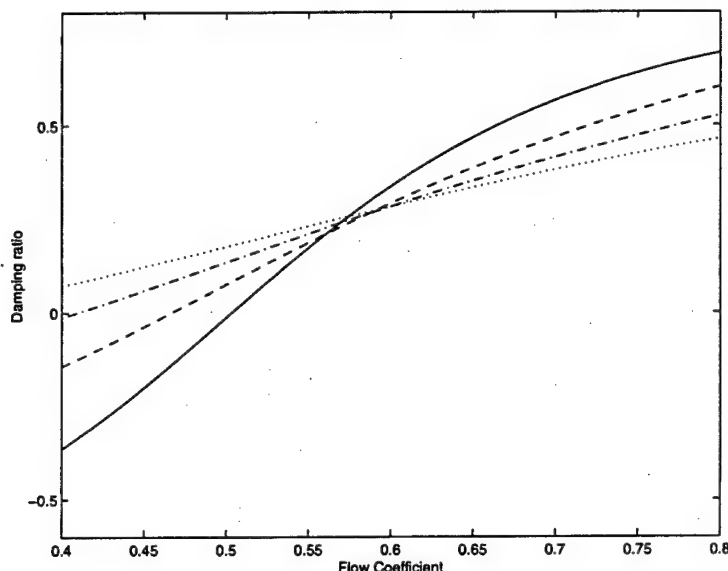
49

Figure 25: Damping ratios of stall for lagged loss, short inter-bladerow space and effectively rigid blades. — 1st mode, – – 2nd mode, – · 3rd mode, · · · 4th mode. All other parameters take their nominal values.

of the stall mode changes as the bladerows become effectively de-coupled or it could simply be an artifact of the Pade approximant used in the modeling of the perturbation flow field (section 2.7). For large values of L_{ibs}, the stall modes are found to have much higher frequencies and less damping. Though not shown here, the root loci of the flutter modes are found to be continuous over this range of L_{ibs}.

6.7 Inlet total pressure

The nondimensional inlet total pressure will vary with operating conditions. In particular, it increases with both airspeed and temperature. Flutter is sensitive to inlet total pressure but stall is not. The dependence of flutter damping on inlet total pressure is illustrated in figure 32. Increased inlet total pressure is shown to destabilize the forward-traveling modes and the first backward-traveling mode, the other backward-traveling modes are stabilized, and there is no influence on the eighth nodal diameter mode.
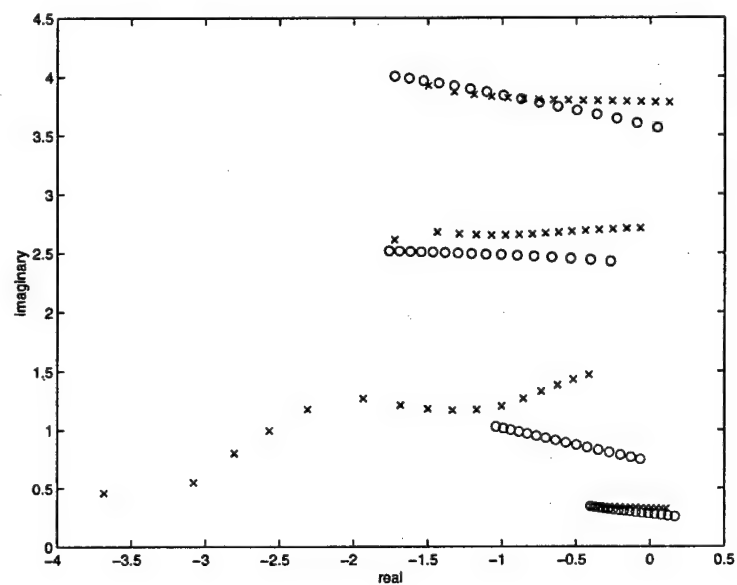
Figure 26: Root locus of stall eigenvalues as flow coefficient varies from 0.4 to 0.8 for lagged loss × and for steady loss ∘. All other parameters take their nominal values.
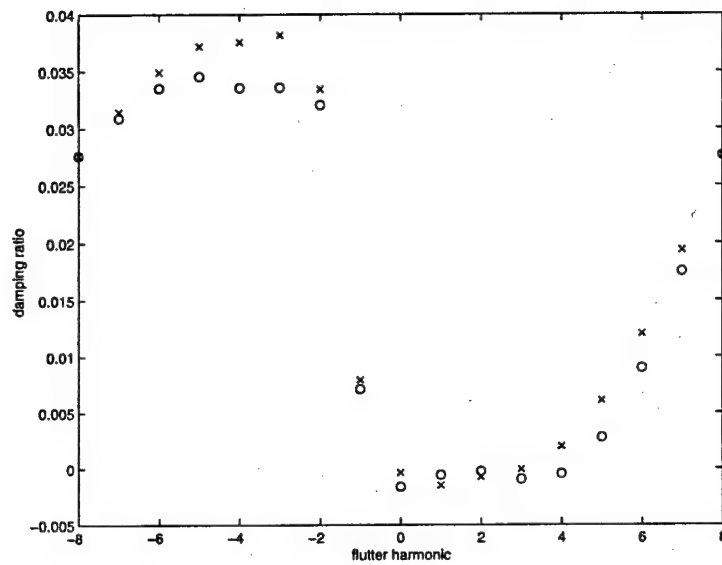
Figure 27: Sensitivity of flutter damping to unsteady losses; lagged loss ×, steady loss ∘. The flow coefficient is given by $\Phi = 0.55$. All other parameters take their nominal values.

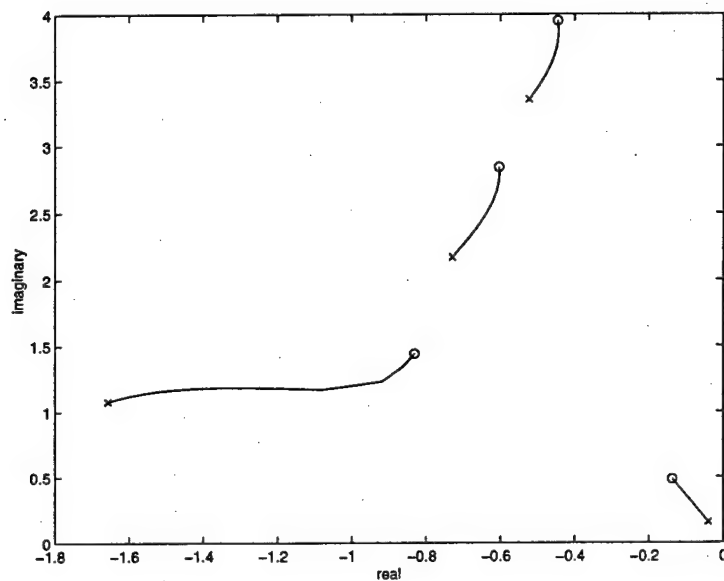Figure 28: Root locus of stall eigenvalues as α_{inlet} is varied from 0 o to 2 ×. The flow coefficient is given by $\Phi = 0.55$. All other parameters take their nominal values.
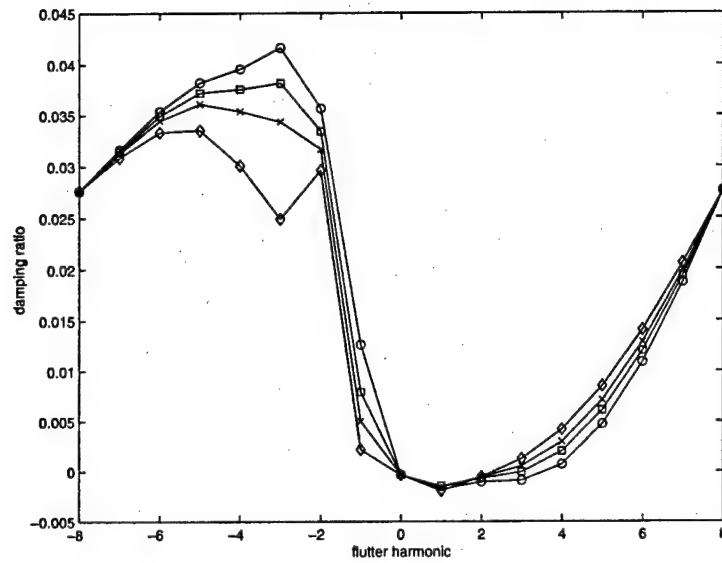
53

Figure 29: Effect of α_{inlet} on damping ratios of flutter modes. α_{inlet} takes the values 0 ∘, 0.5 □, 1 ×, and 2 ⋄. The flow coefficient is given by $\Phi = 0.55$. All other parameters take their nominal values.
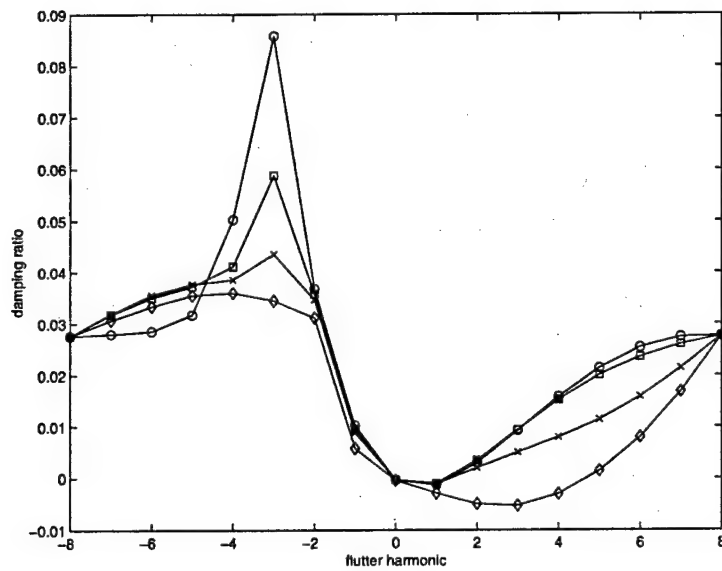
54

Figure 30: Dependence of flutter damping ratios on length of the inter-bladerow space, L_{ibs}. L_{ibs} takes the values 2×10^{-3} ○, 0.1 □, 0.2 ×, and 0.5 ◇. The flow coefficient is given by $\Phi = 0.55$. All other parameters take their nominal values.
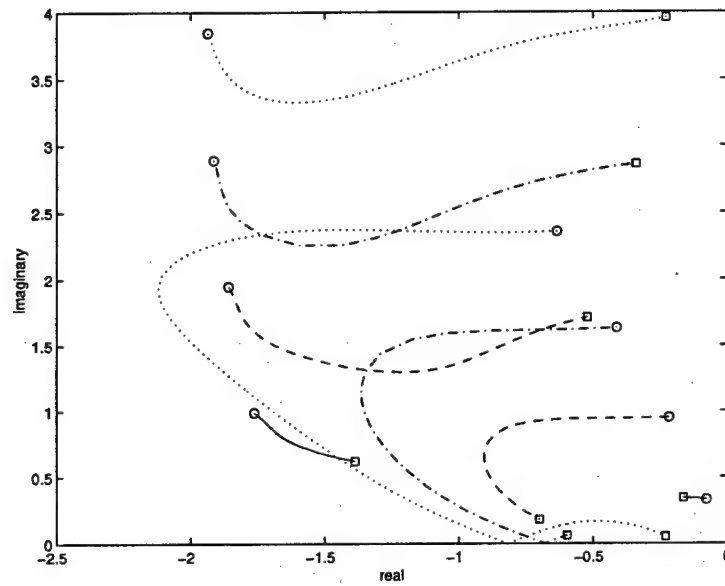
Figure 31: Root locus of stall eigenvalues as length of the inter-bladerow space is varied. L_{ibs} varies from 2×10^{-3}, o, to 0.5, □. The flow coefficient is given by $\Phi = 0.55$. Blades are effectively rigid, all other parameters take their nominal values.

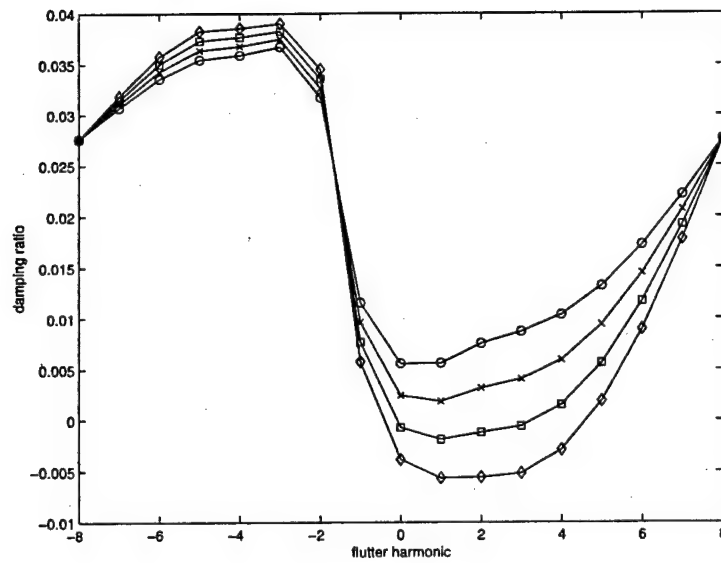Figure 32: Dependence of flutter damping ratios on inlet total pressure, P_{atm}. P_{atm} takes the values 1.5 ∘, 2.0 ×, 2.5 ▫, and 3.0 ◇. The flow coefficient is given by $\Phi = 0.55$. All other parameters take their nominal values.

7 System identification and control

Experimentally, system stability may be evaluated from its forced response. In this section, the role of actuation in system identification is investigated. Mass flow actuation will be used to drive the system, system output which will be examined include pressure at the rotor trailing edge, blade deflection in the rotor frame (such as might be measured with a strain gage), and blade deflection in the stator frame.

The DAE system is of the form

$$\Delta(x, \dot{x}, \xi) = 0,$$

where ξ represents the modal amplitudes of the bleed mass flow. For a particular choice of the actuation ξ, the system transfer functions can be found by first linearizing the system and assuming a time dependence of the form $x = x_0 \exp(st)$,

$$[s\Delta_{\dot{x}} + \Delta_x] x + \Delta_\xi \xi = 0.$$

This is a linear algebra problem of the form $Ax = b$ where $A = s\Delta_{\dot{x}} + \Delta_x$ and $b = -\Delta_\xi \xi$. The matrix A may be singular in which case a minimum least-squares solution may be found using the singular value decomposition. If the actuation vector ξ is chosen to have unit magnitude, then the transfer functions are given by the solution x.

The transfer functions inherit the linear independence of the different azimuthal harmonics. For example, consider the static pressure downstream P_{2a} from the rotor as the output. The modal expansions of the bleed mass flow rate and pressure P_{2a} are then

$$\xi(\theta, t) = \xi_{0rl} + \sum_{k=1}^{N} \xi_{krl} \cos(k\theta) - \xi_{kim} \sin(k\theta)$$

$$P_{2a}(\theta, t) = P_{2a,0rl} + \sum_{k=1}^{N} P_{2a,krl} \cos(k\theta) - P_{2a,kim} \sin(k\theta).$$

In the case of *modal* actuation, only a single pair of amplitudes ξ_{krl}, ξ_{kim} is nonzero. It can easily be shown that the output responds only in that same mode, $P_{2a,jrl} = P_{2a,jim} = 0$, for all $j \neq k$. Further, there is only one independent transfer complex function G_k between the inputs and outputs:

$$\frac{P_{2a,krl} + iP_{2a,kim}}{\xi_{krl} + i\xi_{kim}} = G_k(s).$$

Point-to-point transfer functions refer to the response of a particular sensor to a particular actuator. In this case, a single bleed valve located at $\theta = \theta_b$ is actuated,

$$\xi(\theta, t) = \xi_p e^{st} \delta(\theta - \theta_b).$$

The delta function may be expanded in a Fourier series,

$$\xi_p\, e^{st}\delta(\theta - \theta_b) = \xi_p\, e^{st} \left[\frac{1}{2\pi} + \frac{1}{\pi} \sum_{k=1}^{N} \cos(k\theta_b)\cos(k\theta) + \sin(k\theta_b)\sin(k\theta) \right].$$

Superposition applies and the response of a particular pressure sensor at $\theta = \theta_p$ is found to be

$$p(\theta_p, t) = \xi_p\, e^{st} \left[\frac{G_0}{2\pi} + \frac{1}{\pi} \sum_{k=1}^{N} G_k \cos(k\theta_b - k\theta_p) \right].$$

in terms of the modal transfer functions.

Of particular interest is the transfer function between blade deflection and a travelling wave generated by bleed actuation. The flutter and stall modes are both travelling-waves. Travelling-wave excitation would take the form,

$$\xi(\theta, t) = \xi_k \cos(k\theta + \omega t + \phi).$$

In the present model formulation, the rotor has angular velocity -1. *Forward-travelling* waves travel in the same direction as the rotor, hence, $k > 0$ corresponds to forward-travelling waves and $k < 0$ corresponds to backward travelling waves. A transfer function $G_k(\omega)$ can be found such that the blade deflection (measured in the stator frame) will be given by

$$\alpha(\theta, t) = G_k(\omega)\xi_k \cos(k\theta + \omega t + \phi).$$

If ψ is taken to be the azimuthal coordinate fixed to the rotor frame, the coordinate transformation will be given by $\theta = \psi - t$. The blade deflection in the rotor frame, which could be measured with a strain gage, is then given by

$$\alpha_{\mathrm{r}}(\psi, t) = G_k(\omega)\xi_k \cos[k\psi + (\omega - k)t + \phi].$$

The transfer function between any output and any input contains stability information about all of the system eigenmodes. In practice however, it is important to choose actuation that acts strongly upon the eigenmode of interest. Otherwise the information may be lost in experimental noise. It is also important to select sensors for which the direct effect of actuation is comparable to or smaller than the response due to excitation of the system mode. This is evident in the present model. Blade deflection is clearly a good measure of the flutter instability. Suppose blade deflection and mass flow actuation are related by a transfer function G,

$$\alpha = G(s)\xi.$$

If G were approximated by a ratio of polynomials, the roots of the numerator, the *zeroes*, would be well-separated from the roots of the denominator, the *poles*. This implies that if the excitation is very small, the response might still be large

in the neighborhood of the poles. The poles are identical to the eigenvalues of the unforced system. The experimentally measured transfer function can then be used to estimate system eigenvalues. Alternatively, consider how system stability might be interpreted from the transfer function between trailing-edge pressure and mass flow actuation. Blade deflection alone will influence pressure to some degree; mass flow actuation alone will have a much greater impact, thus

$$p = A\alpha + B\xi,$$

where $B \gg A$ over the frequency range of interest. The measured transfer function between pressure and mass flow actuation will then be

$$p = (AG + B)\xi.$$

Representing G as a ratio of its numerator and denominator $G = N/D$,

$$p = \frac{AN + BD}{D}\xi.$$

Since $B \gg A$, the transfer function will have zeros very near the poles associated with flutter. Coupled with noise, this greatly complicates the task of estimating the poles from the experimentally obtained transfer functions. As an example, transfer functions between blade deflection and mass flow and between trailing-edge pressure and mass flow for second nodal diameter, forward-travelling flutter are illustrated in figures 33 and 34. The blade deflection transfer function indicates the classic response of a forced oscillator. In contrast, the "kink" in the pressure transfer function is consistent with pole-zero cancellation. Rational polynomials have been fit to the curves to illustrate how one might estimate system stability information from experimentally-measured transfer functions.

From the model, the poles and zeros may be computed directly for either source of outputs. The poles, of course, won't change. Returning again to the linearized DAE system,

$$[s\Delta_{\dot{x}} + \Delta_x]x + \Delta_\xi\xi = 0,$$

the poles correspond to values of s which satisfy the linearized system when $\xi = 0$. Likewise, the zeros correspond to values of s which satisfy the linearized system when the output $y = Ax = 0$. Each case can be solved as an eigenvalue problem, the poles are given by the eigenvalues of the matrix

$$[s\Delta_{\dot{x}} + \Delta_x],$$

and the zeroes are given by the eigenvalues of the matrix

$$\begin{bmatrix} (s\Delta_{\dot{x}} + \Delta_x) & \Delta_\xi \\ A & 0 \end{bmatrix}.$$

The actual values for the poles estimated in figures 33 and 34 are $0.00132 \pm 3.80i$; the actual values for the zeroes estimated in figure 34 are $-0.0947 \pm 3.83i$.
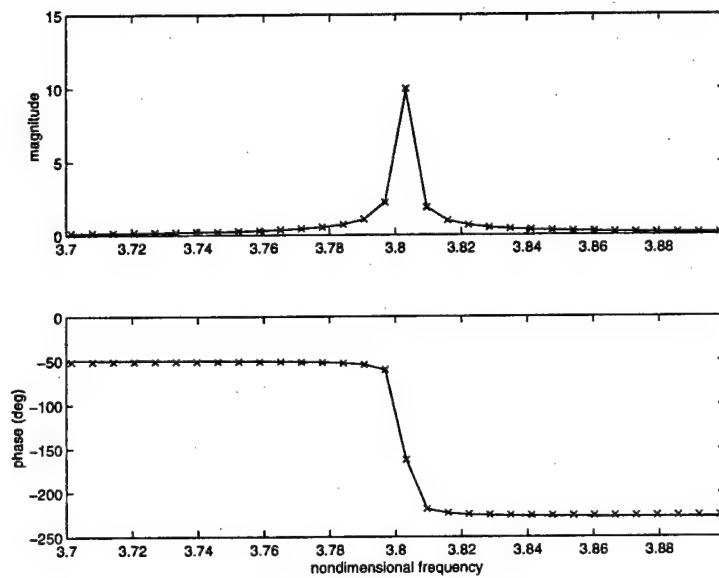
60

Figure 33: Transfer function between blade deflection and mass flow actuation, 2nd nodal diameter, forward-travelling flutter mode. — indicates a fit using 2 poles and 2 zeroes. Estimated eigenvalues: $0.00125 \pm 3.80i$; estimated zeroes: 7.10 and -0.903.
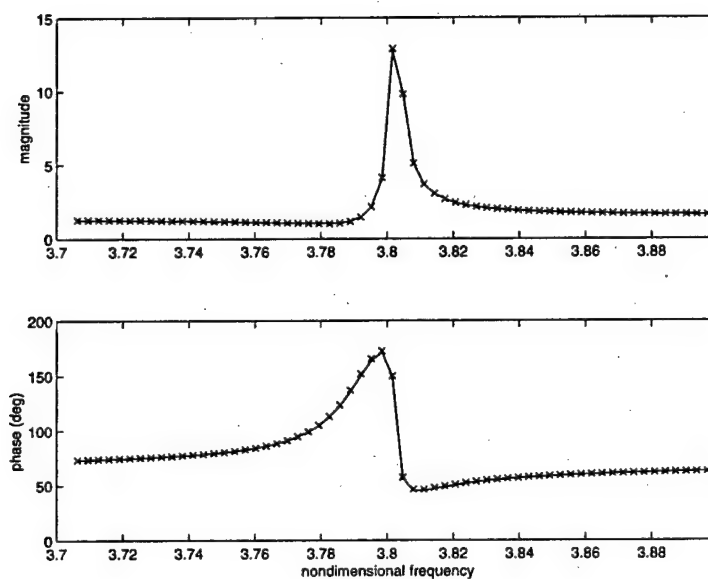
Figure 34: Transfer function between trailing-edge pressure and mass flow actuation, 2nd nodal diameter, forward-travelling flutter mode. — indicates a fit using 2 poles and 4 zeroes. Estimated eigenvalues: $0.00120 \pm 3.80i$; estimated zeroes: $0.0110 \pm 3.79i$, 23.5, and 2.35.

8   Passive control

Based on the observation that flow perturbations and blade deflection are cou-
pled, it is plausible that blade deflection can be treated indirectly by adding
damping to the flow perturbations. In this section, Helmholtz resonators are
examined with regard to passive control of flutter. Consistent with the assumed
form of mass flow actuation, it is desirable that passive dampers act on all flutter
modes. This can be accomplished by distributing Helmholtz resonators finely
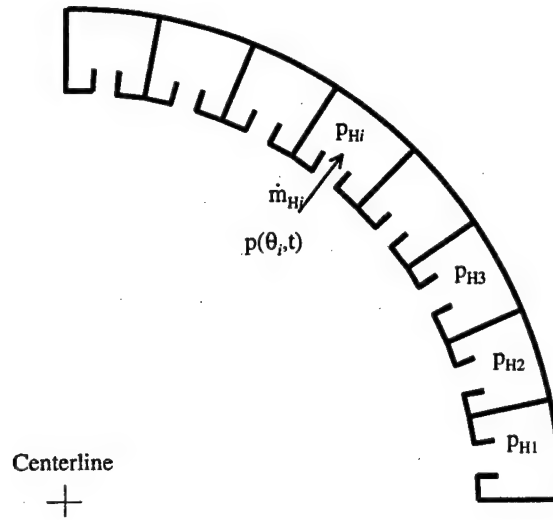and evenly around the casing as in figure 35.

Figure 35: Schematic of Helmholtz resonators for passive control, 1/4 annulus.

Considering a single resonator, the conservation of mass within the plenum
may be expressed

$$\frac{V}{c^2}\dot{p}_i = \dot{m}_i,$$

where p_i is the pressure within the plenum, $\dot{m}_i$ is the mass flow into the plenum,
V is the volume of the plenum, and c is the sonic velocity. The conservation of
momentum within the neck of the resonator may be expressed

$$l\frac{d\dot{m}_i}{dt} = [p(\theta_i, t) - p_i]A - \kappa\dot{m}_i,$$

where $p(\theta_i, t)$ is the pressure directly outside the plenum, l is the length of the
neck, A is the cross-sectional area of the neck, and κ is a viscous loss constant. In

the limit of a continuum of small oscillators, these equations may be combined
and nondimensionalized to obtain the oscillator equation

$$\ddot{\xi} + 2\zeta_H Q_H \dot{x} i + Q_H^2 \xi = \beta_H \dot{p}_{2b}. \tag{33}$$

The damping ratio is given by ζ_H and Q_H is the ratio of the Helmholtz resonator
frequency to the shaft frequency; the gain $\beta_H = A/(\pi R_{nom} l)$. The DAE system
(30) is augmented by equation (33) and the mass flow actuation parameters now
become state variables.

9 Mistuning

It has been noted that the linearized governing equations de-couple by the Fourier harmonics. This is a consequence of azimuthal symmetry. If that symmetry is broken, there will be some coupling of the Fourier harmonics in each of the stall and flutter mode. One might reasonably hypothesize that this coupling would lead to increased damping in the least damped modes and decreased damping in the most damped modes. A negative aspect of mistuning is that any disturbance will excite all of the modes to some degree. The forced-response of the system will then be larger.

Mistuning has been incorporated into the reduced-order model by allowing for variability in blade stiffness and by allowing for variability in the stagger angle. First, the equations of motion were re-derived in the rotor frame of reference. Secondly, the stagger angle γ_r and the blade stiffness parameters Q_b and Q_t were expanded as Fourier series in the rotor-frame azimuthal coordinate ψ. The Galerkin projection over the azimuthal angle becomes excessively tedious to accomplish using symbolic algebra. Collocation (as in the stall model of Mansoux *et.al.* [7]) has been used thus far, but results are not satisfactory. In the future, numerical integration over ψ will be pursued.

The present approach to mistuning is novel in that it considers mistuning of the complete aeromechanical system. One consequence of mistuning is that a steady solution exists only in the mistuned frame. If for example the blade stiffness is mistuned, the steady deflection will be a function of the angle ψ. In the stator frame, the observed blade deflection will be periodic over a blade rotation. Another consequence is that the blades will react differently to the aeroload and, conversely, the flow perturbations will be influenced by the variable blade defection. All of the consequences are accounted for in the reduced-order model.

10 Nonlinear interaction of stall and flutter

In addition to local stability, one must also consider stability with respect to finite amplitude perturbations. Below in figure 36 are plotted time histories of stall and flutter, respectively. obtained by numerically integrating the DAE system. The instabilities occur as Hopf bifurcations and also break azimuthal symmetry. The amplitude saturation is due to nonlinearity. As revealed in these plots, flutter and stall are typically coupled.

Rotating stall typically occurs as a hard loss of stability or subcritical Hopf bifurcation. There exist a range of parameters near the stability boundary for which the system is locally stable but unstable to finite perturbations. This has been observed in practice and in experiments. Supposing the engine is tested along a speedline, the system enters stall near the compressor peak but only recovers from stall when the operating point is returned to much lower pressure
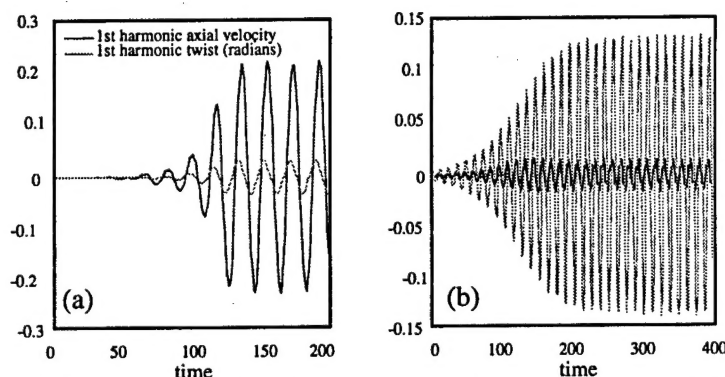
Figure 36: (a) Time history of stall oscillations, (b) Time history of flutter oscillations.

ratios. Thus far, flutter instability has been found to be a soft loss of stability or supercritical Hopf bifurcation. A numerically generated bifurcation diagram is plotted in figure 37 along with the locus of fixed points (speedline). The throttle parameter A is slowly varied in time; in these simulations a small noise perturbation has been added to the first harmonic of the inlet flow coefficient. Initially, the throttle parameter is gradually decreased from a suitably large value at which the system is stable. As A is decreased, the equilibrium point moves up the speed line and the system loses stability through flutter at a flow coefficient of $\Phi_f = 0.564$. The apparent gap between flutter instability and saturation of the flutter limit cycle is due to the fact that the growth rate is initially so small that the variation of A does not appear quasi-steady. At $\Phi \approx 0.525$ the trajectory leaves the flutter limit and settles onto the stall limit cycle. The throttle parameter is then gradually increased back to its initial value. Co-existent flutter and stall limit cycles are demonstrated between $\Phi = 0.52$ and $\Phi = 0.55$. The turning point of the stall limit cycle is apparently at $\Phi \approx 0.55$, well above the point of linear instability at $\Phi_s = 0.536$. Below this turning point, the stall limit cycle does not exist and the trajectory quickly drops back onto the equilibrium point before gradually cycling back up to the flutter limit cycle. This plot demonstrates hysteresis between flutter and stall limit cycles. If the flutter instability were not present, hysteresis between the stall limit cycle and the equilibrium curve would exist in the range between the point of stall instability and the turning point of the stall limit cycle.

In future work, normal forms of the dynamical system will be interpreted from simulations following the example of Anderson *et.al.* [1]. This will allow
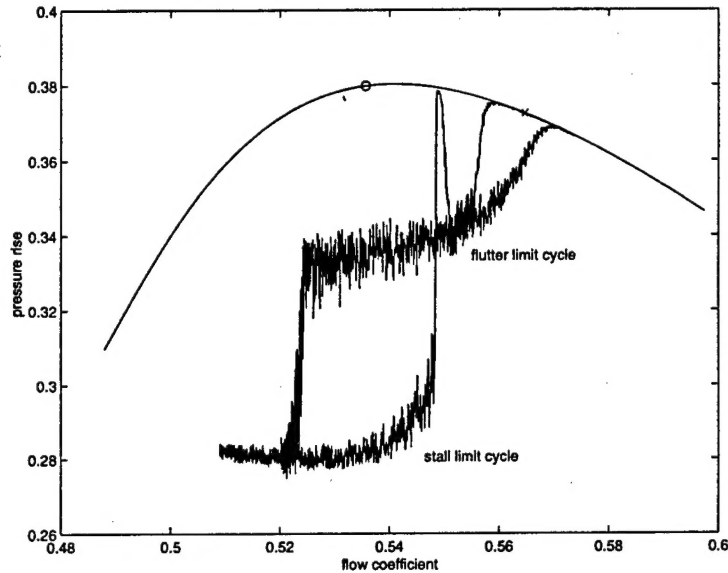
66

Figure 37: Numerical bifuration diagram demonstrating hysteresis between stall and flutter limit cycles due to subcritical Hopf bifurcation. × indicates point of flutter instability, o indicates point of stall instability.

an analytical approximation of the unstable branch of the stall limit cycle and analysis of codimension-2 bifurcations.

11   Conclusion

A reduced-order model representing a unified view of the stability of flexibly bladed compression systems has been described. The model captures the essential nonlinear coupling between surge, rotating stall and flutter, and provides a vehicle for the systematic investigation of their interaction. The approach to model construction described above provides a tractable qualitative yet physically-based dynamical description of the interaction of performance-limiting compression system instability phenomena. Analysis of the linear stability boundaries is consistent with operability limits observed in practice for turbomachinery. The post stall and flutter behavior simulated is also consistent with experimentally observed behaviors.

67

References

[1] Anderson, J.S., Kevrekidis, I.G., Rico-Martinez, R., and Krischer, K. 1996 Use of adaption and feedback in the experimental detection of bifurcations. *Proceedings of the 30th Annual Conference on Information Sciences and Systems, IEEE,* **1**:155–160.

[2] Copeland, G.S. 1997 Reduced-order DAE models for turbomachinery stall, surge, and flutter. *Annual meeting of the Gesellschaft für Angewandte Mathematik und Mechanik,* March 24-27, Regensburg, Germany.

[3] Greitzer, E.M. 1998 Personal communication.

[4] Gysling, D.L. and Myers, M.R. 1996 A framework for analyzing the dynamics of flexibly-bladed turbomachines. *ASME 96-GT-440. Intl. Gas Turbine and Aeroengine Congress and Exhibition,* Birmingham, U.K., June 10-13, 1996.

[5] Haynes, J.M., Hendricks, G.J., and Epstein, A.H. 1994 Active stabilization of rotating stall in a three-stage axial compressor. *Journal of Turbomachinery.* **116**:226–239.

[6] Longley, J.P. 1994 A review of nonsteady flow models for compressor stability. *Journal of Turbomachinery.* **116**:202–215.

[7] Mansoux, C.A., Gysling, D.L., Setiawan, J.D., Paduano, J.D. 1994. Distributed nonlinear modeling and stability analysis of axial compressor stall and surge. *Proceedings of the 1994 American Control Conference,* June 29 – July 1. Green Valley, Arizona, USA. **2**:2305 – 2316.

[8] Moore, F.K. and Greitzer, E.M. 1986. A theory of post-stall transients in axial compression systems: parts I and II. *ASME Journal of Engineering for Gas Turbines and Power.* **108**:231–239.

[9] Smith,B.T., Boyle, J.M., Dongarra, J.J., Garbow, B.S., Ikebe, Y., Klema, V.C. and Moler, C.B. 1976. *Matrix Eigensystem Routines — EISPACK Guide,* Springer-Verlag.

[10] Wong, M.T.M. 1997 *System Modeling and Control Studies of Flutter in Turbomachinery.* MS Thesis, Massachusetts Institute of Technology.